The Pennsylvania State University

The Graduate School

Department of Physics

GRAVITATIONAL WAVES FROM INTERMEDIATE MASS BINARY BLACK HOLES: FIRST STEPS TOWARD USING NUMERICAL RELATIVITY WAVEFORMS FOR LIGO DATA ANALYSIS

A Thesis in

Physics

by

Birjoo Dilipkumar Vaishnav

Submitted in Partial Fulfillment
of the Requirements
for the Degree of

Doctor of Philosophy

August 2008

The thesis of Birjoo Dilipkumar Vaishnav has been reviewed and approved[⋆] by the following:

Deirdre Shoemaker
Assistant Professor of Physics
Thesis Adviser
Chair of Committee

Ben Owen
Assistant Professor of Physics

Pablo Laguna
Professor of Physics and Astronomy
Astrophysics

Richard Wade
Associate Professor of Astronomy
Astrophysics

Jayanth Banavar
Professor of Physics
Head of the department

[⋆] Signatures are on file in the Graduate School.

Abstract

The need for providing accurate and reliable templates for detecting gravitational waves from the LIGO and LISA gravity wave detectors has fueled the numerical relativity effort toward solving the binary black hole problem. The waveforms from these simulations are vital in extending the mass reach of the ground based detectors to include the intermediate mass black hole binaries ($M > 50M_{\odot}$). The aim of this thesis is to study some aspects of how the merger waveforms from a variety of initial configurations look under the eyepiece of data analysis. We study waveforms from equal mass binary black holes which are initially non-spinning, spinning without precession and spinning with precession in quasi-circular orbits. The mode content for these waveforms is found to behave within the expectation set by the post-newtonian theory. Also studied are waveforms from a number of initially non-spinning, equal mass binaries in eccentric orbits. One of the results of the thesis investigation is that for intermediate mass black hole binaries a quasi-circular non-spinning template may be effective in capturing low and moderate eccentricity waveforms. The analysis can be useful in guiding the set up of a detection template bank for observing mergers of intermediate mass binary black holes with ground based detectors.

Table of Contents

List of Tables

List of Figures

Acknowledgments

It was a fine afternoon about a decade and a half ago when I bought a paperback copy of Hawking's celebrated book "A brief history of time" which led me to seek a career in physics, eventually leading up to this thesis. Looking back, it is humbling to see the innumerable number of individuals whose support as friends, teachers and mentors has made this academic journey possible. This is my humble attempt to thank many but not all of the individuals who played a vital part directly or indirectly in making this thesis happen.

My adviser Dr. Deirdre Shoemaker, was a constant source of encouragement and organization of ideas and time. I hope to someday be as good a communicator and presenter as she is. Am really grateful to her for all her trust in me and the freedom she gave me to explore at a vital time in my career.

Interactions with Prof. Pablo Laguna taught me that one of the most important attitudes for success in research is to look at what can be done with what is available, instead of letting the lack of resources stop you. His and my adviser's patience with my crazy ideas and support of reasonable ones is very much appreciated. Am grateful to Prof. Ben Owen for support and encouragement and advice about the numerous issues in data analysis and post-Newtonian theory and various other issues in the thesis.

Am also indebted to Prof. David Weiss, my adviser in my brief stint in experimental atomic physics, for teaching me that attention to details is an indispensible prerequisite for good science. He was a great mentor who at a vital time reminded me to think about the long-term goal and my passion, which eventually led me back to gravity. In part this thesis owes to Prof. Abhay Ashtekar who was my first mentor at Penn State and who has been a great source of inspiration and support. Am grateful to him for suggesting Prof. Shoemaker as a possible adviser when I wanted to return to gravity theory. Also am grateful to: Prof. Lee Sam Finn for his patient and insightful guidance, Prof. Jayanth Banavar for his patient listening and guidance at various points in my career at Penn State and Prof. Richard Wade for taking the time to carefully read the thesis and asking stimulating questions.

There are several colleagues in the physics community at Penn State and elsewhere who made this endeavor fun, among whom are my collaborators Frank Herrmann and Ian Hinder, colleagues in no particular order: Tanja Hinderer, Eloisa Bentivegna, Nico Yunes, Xiao Li, Nathan Urban, Mohit Nayyar, Ravi Koparappu, Alberto Sessana, Emanuele Berti, Richard O'Shaughnessy, Shantanu Desai, Malik Rakhmanov and Carlos Sopuerta.

My so many friends all over the world in the International Association for Human Values and the Art of Living foundation who tirelessly encouraged me to reach the light at the end of the tunnel (which appeared to be switched off at times). In particular, Gokul Kandiraju, Deepak Ramrakhyani, Murali Vilayannur, Partho Nath, Amitayu Das, Lakshmi Gopinathan, Kiranmayi, Ishanu, Venkat, Mukesh, Jagadish, Chris Ambrose, the Dornich family, Ms. Kelly Keefe, Beth Spicer, Mrs. Kat Alden, Amit Ailiani, Lav Rai, Nityanand, Amitayu.

Ofcourse, I have to mention Ms. Randi Neshteruk, Ms. Kathy Smith and Ms. Megan Meinecke for their ready willingness to help and patience with my ineptness in administrative matters. I am unable to imagine how would I have made it without their help.

My mother, Shrimati Hansa D. Vaishnav, is my first mentor alongside my father Shri Dilip H. Vaishnav. Through my early years at home, they instilled into me a thirst for knowledge, learning and a deep respect for nature and its laws. Am eternally grateful for their love and support. I am very grateful for the love of my little brother Dr. Hardik D. Vaishnav, a medical doctor who is almost too wise for his age. Through a major portion of grad school Ms. Heidi Parker supported me with her love and encouragement and am very grateful for her presence in my life.

They say success is 90% perspiration and 10 % inspiration. The most revitalizing dose of inspiration I used to get was from the quietness generated by the knowledge and meditation courses given by His Holiness Sri Sri Ravi Shankar. Words are not enough to thank him for his insightful teachings of meditation and breathing techniques and the art of living which have been a source of nourishment to me at all levels including physical, mental, emotional and spiritual. Several years ago when I was frustrated with string theory and quantum gravity, I asked what he thought about my desire to drop out from grad school and do social service. He said " We move from one success to another, not from one failure to another". Somewhere I was running away from the hard work that goes behind making science and scientific enterprise so powerful and feel gratified at having taken his advise.

Time and again when I was tired and burnt out in research, his techniques to quieten the mind helped me to an extent I could not have imagined apriori. His "Sudarshan Kriya" breathing technique has enabled me over and over again to dissolve stresses and to be at peace even amidst the ups and downs of personal life went during the years of graduate school. Am also indebted deeply to my first "Art of Living" teacher Ms. Iti Samal, Swami Brahmateja, Vikram Hazra, Philip Fraser, Ms. Rajshree Patel, Swami Pragyapad and several other Art of Living teachers. To anyone even remotely curious about the joys of quietness, I would highly recommend learning this technique taught in the Art of Living courses worldwide. Thanks are also due, to the countless number of unnamed volunteers who work with diligence and enthusiasm to support and share this knowledge in an endeavor to create a stress free violence free society. May they be successful in bringing joy and clarity to as many minds as possible.

Chapter 1

Introduction

About a century and a half ago, Maxwell's equations of electromagnetism were published. Their prediction of the existence of electromagnetic waves was verified by hertz in 1886, a couple of decades after the prediction. Today over hundred years later, this prediction has been instrumental in revolutionizing the modern world and it would be hard to imagine a world or a communication system without a theoretical or empirical understanding of electromagnetic waves.

About half a decade after Maxwell's unification of the electric and magnetic fields, Einstein was successful in creating a theory of gravity consistent with the relativity principle, a.k.a equivalence principle. The verification of Einstein's prediction of the bending of starlight by Eddington and his team in 1919 was but a beginning in a series of spectacular triumphs of general relativity in the experimental tests. However there was one prediction which took slightly longer to verify, and even so, has only indirectly been verified till date. This was the existence of gravitational radiation, predicted by Einstein soon after arriving at his equations. It was only about sixty years later that Hulse and Taylor measured the rate at which the orbital period of binary pulsars decays, and showed it matched the expectation from the energy loss to gravitational radiation to within 0.3%. [35]

The quest for a direct detection of gravitational waves, which was pursued for many years by physicists such as Joseph Weber using bar detectors, has remained unsuccessful. This is in part because gravity is a weak force, thirty-seven orders of magnitude weaker than electromagnetism. The other factor that makes the gravitational radiation weak is that unlike in electromagnetism, wherein the changes in electric dipole moment source the radiation, the dipole moment in the gravitational case is momentum, which is locally conserved. The analog of the magnetic dipole moment being the angular momentum, which is another conserved quantity, the first dominant source of radiation turns out to be quadrupolar. Owing to all these factors the potentially observable sources of gravitational radiation tend to be astrophysical in nature and the strains they would cause in detectors would be of the order of thousandths of nuclear diameter.

1.1 Gravitational Radiation, Sources and Detection

With the advances in interferometry, it was possible to imagine attaining measurement accuracies which would be enough to detect the minuscule strains that astrophysical sources would induce on ground-based detectors. The size of the ground based detector constrains the sources of this radiation and how many of those are expected in some astronomical volume accessible to the detector. It turns out that compact object binaries consisting of neutron star-black hole or binary black holes or even supernovae can be strong sources for LIGO. Merger rate estimates for such mergers indicate that while the expected detection rate for initial LIGO is small, that for the advanced LIGO could be as high as one event per week.

The next question is to see how to look for gravitational waves in the detector data stream. The foundations of gravitational wave astronomy for these gravitational wave detectors was laid by [25, 30, 31]. For an unknown signal such as a supernova, there are various statistical methods like excess power, MaxEnt etc, which drive the burst searches over the LIGO data. On the other hand when the form of the signal is known a-priori, the best method for extracting the signal from noise is that of matched filtering. For stellar mass sources the inspiral part of the signal is well approximated by the restricted post-newtonian approximation, which is believed to provide a waveform, potentially up to the innermost stable circular orbit frequency. For sources of a higher total mass, the final merger and ringdown become significant.

While most black holes formed out of stellar collapse are typically of tens of solar masses, the existence of the so called intermediate mass black holes is a subject of ongoing debate. There are suggestions from observations which are yet to be well-established, that there may be several intermediate mass black holes ($50 \leq M/M_{\odot} \leq 400$) in galactic clusters. Hierarchical merger scenarios of galaxy formation suggest that the super massive black holes at the centers of galaxies can form by runaway mergers of binaries formed in clusters and the subsequent mergers of galaxies.

If such intermediate mass binaries exist, the majority of gravitational wave signal from them will come from the last few orbits prior to their coalescence and the subsequent ringdown. The frequency of the gravitational waves from a non-spinning or non-precessing spinning binary increases monotonically, and hence the higher the mass of the black hole, more relevant the merger part gets to the detection.

To know the final state of the merger or also the exact time of coalescence of the binary would require a solution of the full Einstein equations. Solving the trajectories and extracting the waveforms for this coalescence of binary black holes became the challenge for numerical relativity for over a decade, and only in the last couple of years there has been a breakthrough in obtaining waveforms for the coalescence of the binaries.

1.2 The numerical relativity binary black hole waveforms

The numerical simulations of binary black holes need to be carried out via supercomputers and for a long time it was difficult to avoid the code from crashing. In 2005, Bruegmann et al [10] evolved the first orbit or so although the code crashed before merger. Soon after, Pretorius [4] was successful in evolving several orbits of the binaries,approaching the problem from an entirely different method. This code was both stable and demonstrated numerical convergence. Before the successful availability of these waveforms, it was difficult to get an accurate and reliable estimate of the parameters of the black hole produced upon coalescence of the binary starting from some initial configuration. Although there were some attempts to make analytical estimates of the final state from approaches such as the *effective-one body approach*[44], the results were not accurate enough to provide reliable results for data analysis. The availability of these waveforms from the last few orbits opens up several possibilities in gravitational wave astronomy in the strong field, especially for the higher mass black holes. In fact soon after Pretorius[46] there was a flurry of activity, [16, 23] in the numerical relativity community in which several groups were suddenly able to evolve long and stable binary black hole evolutions just by slightly modifying their original approach.

1.2.1 Parameter Space of numerical relativity simulations

The first numerical relativity simulations considered equal mass, non-spinning black holes as this is the most symmetric situation, and hence easiest to simulate in terms of computational resources required. In general, given two black holes, each could have a separate spin magnitude and orientation, a non=unit mass ratio, and possibly an initial eccentricity. Together this would mean eight parameters $(\eta, a_1, a_2, \mathbf{s_1}, \mathbf{s_2}, e)$. In an world with infinite computing power at hand one would simply run the simulations for all these parameters, locate the points in evolution up to which post-newtonian approximation is valid as a function of each of these parameters, and then use the "hybrid" waveforms that cover the "complete" regime of inspiral, merger and ringdown for searching over the gravitational wave detector data.

Of course in real life the resources are limited, and it is not clear that one needs to run all these simulations in order to detect the final orbits of a generic binary black hole. It might be that just a few of these waveforms encode enough information to serve as a basis for example, in detecting a generic waveform. Although this sounds unlikely, a related question that would need to be answered is what is a minimal set of initial waveform parameters for numerical relativity that need to be run in order to ensure the detection of a generic astrophysical merger?

The one parameter which is intrinsic to the black holes but not mentioned above is the mass of the black holes. The reason why mass was left out was because the form of the Einstein equations which are numerically evolved is chosen to be in a mass-scale independent form. As a result all the variables including space and time co-ordinates can be accordingly re-scaled for systems of different masses, the number of cycles and orbits being the invariants because the initial separations would also scale with mass.

The frequency at which the merger occurs is inversely proportional to the mass. And the merger of stellar mass black holes occurs at frequencies higher than the sweet spot of the sensitivity of the interferometer. The mass of the black holes for which the merger occurs at the sweet spot of the interferometer and hence for which the numerical relativity waveforms are most relevant for gravitational wave detection with ground based detectors, is of the order of $50 - 200M_{\odot}$. For the advanced detectors this range will increase but the qualitative dependence of the various data analysis quantities on the intrinsic parameters will have similar trends for both advanced LIGO as well as LISA. For ease of presentation and approach, we shall just consider the initial LIGO noise curve in this thesis. The generalization to other noise profiles is straightforward. In the next section we shall give an overview of the specific problems addressed in this thesis.

1.3 Numerical Relativity meets Data Analysis

Numerical relativity efforts will benefit from *a priori* knowledge of where best to spend those resources to create an appropriate library of waveforms. Additionally, the cost of doing data analysis for a large template bank with many parameters is also computationally expensive. Knowledge of the sensitivity of the waveforms to the parameters will guide efforts in data analysis and numerical relativity. As the library of numerical relativity waveforms grows, we can determine how the waveforms will be best employed in the search for gravitational waves and the characterization of their sources. They may be used in conjunction with post-Newtonian waveforms through stitching, as templates for binary mergers, or to test the quality of template spaces built from post-Newtonian and/or approximate waveforms.

In [43], a comparison of the closeness between current gravitational wave search template banks and numerical relativity waveforms from non-spinning binary black holes (BBHs) has been performed. The numerical relativity waveforms were used as target signals against which the template banks currently in use by LIGO to search for inspiral gravitational waves were tested. They found matches greater than 0.96 for many of the analytic and approximate template families at $10 - 120 M_{\odot}$. In [1], a phenomenological family of waveforms was proposed to model the coalescence of the BBHs using a hybrid method that combines analytical and numerical relativity waveforms. They achieve matches greater than 0.99 at $30 M_{\odot} - 130 M_{\odot}$ for non-spinning BBHs.

1.4 The layout of the thesis

As we saw in the previous section, there are several initial parameters on which the numerical relativity waveforms depend. The objective of this thesis is to study the impact of these parameters on the application of these waveforms to gravitational wave detection. A toy model study exploring possible issues at this interface, using ringdown waveforms from the Zerilli code, which does not include any noise profile unlike in the case with binary black hole waveforms are studied in chapter two. In chapter three we develop the data analysis toolkit, mathematical formulae etc., that would be needed for the rest of the thesis. One of the first issues that arises before we use these waveforms for inferring their data analysis properties, is that of how accurate they need to be for being used to matched filter a realistic signal from nature. These issues in the context of a LIGO noise profile and binary black holes from non-spinning as well as some spinning anti-aligned and spinning quasi-circular configurations is the subject of chapter four.

As the observer's inclination with respect to the orbital plane of the binary changes, the mode content in the observed waveform changes. Is it enough to use the dominant mode waveform that is used in setting up inspiral template banks for the merger detection case? It turns out that the answer to this depends on the initial configuration of the system. On the data analysis side, sometimes the distinction between the so-called minimax match and the fully phase optimised match isnt clarified, whereas the difference can be quite significant. We investigate these issues for non-spinning and anti-aligned spin waveforms with different initial spin directions in the chapter five.

The waveforms used in the analysis for these cases are short, two to three cycles long waveforms that were generated when the PennState code first became functional, in early part of fall 2006. Longer waveforms became available sometime in 2007, with which one could study other issues like matching to the post-Newtonian approximation as well as in decreasing the lower mass limit up to which these templates would be useful for data analysis. Using the initial data at larger separations, waveforms from binaries in eccentric orbits were generated and they seemed to exhibit a weak dependence of the final spin on the initial eccentricity, for eccentricities as large as 0.4. Owing to this one could imagine being able to detect waveforms with non-zero eccentricity in the final orbits using the quasi-circular merger waveforms that will be used in future searches. This forms the subject of chapter six. In chapter seven we investigate how effective the non-spinning, quasicircular templates are in detecting the spinning waveforms at different observer inclinations, as well as in detecting an optimally oriented eccentric binary source. The conclusions are presented in chapter eight.

Chapter 2

Analyzing Zerilli Waveforms:
A Toy Model

As a precursor to the analysis of numerical relativity waveforms from binary-black-hole mergers, we use numerical ringdown templates generated by a Zerilli code at several resolutions. The aim is to give a first exposure to the concepts of data analysis as they might be applicable for numerical relativity waveforms. The work presented in this chapter upholds this claim and further investigates the role that truncation errors play in creating a template space of numerical waveforms and performing a parameter estimation for a model problem.

Our model problem is that of a perturbed Schwarzschild black hole. The solution to the ringdown is well known in general relativistic perturbation theory, and has been used to create data analysis search algorithms for the ringdown waveforms [40, 52]. We use a code written by Pablo Laguna that solves the spherically symmetric Zerilli equation[60] using finite differencing techniques to produce waveforms that have numerical errors of the same kind as those present in a fully three-dimensional BBH template from numerical relativity. This model has the added advantage that it mimics the end-result of a BBH merger, the ringdown of the final black hole modulo the spin parameter which we have set to zero to keep the parameter space one-dimensional. The notations in this chapter differ slightly from those used for the full numerical relativity calculations that forms the majority of this thesis. Because the calculations in this chapter assume a white noise profile, they are only illustrative of the concepts and not directly applicable to LIGO.

We characterize the numerical errors in our ringdown waveforms through the matched filtering procedure and identify where differences from the analytic case arise. The waveforms are dominated by truncation errors and the outer boundary is causally disconnected from our domain, as is the case in the full 3D BBH code. The model has the advantage that the code is computationally efficient and can be run for large number of resolutions quickly.

Once we used the ringdown waveforms to create a template bank, we found that the coverage over the parameter space was incomplete and would result in loss of events due to the differences between the signal and template manifold caused by the numerical errors. In studying the use of these templates to estimate the parameters of the signal, we found a systematic bias in the estimation of the source parameters at the order of a percent, which means the procedure identified the "wrong" mass. While these effects are small, they may be magnified when using the more complicated numerical BBH waveforms.

The In §2.1 we describe the definitions and formalism for both the data analysis and numerical Zerilli templates that we use throughout this chapter. The efficiency of the template and tiling is given in §2.2. The systematic bias in parameter estimation due to numerical error is presented in §2.3. We summarize and conclude in §2.4.

2.1 The numerical Zerilli waveforms and data analysis formalism

The ringdown of a black-hole spacetime may be detectable by ground-based detectors as it occurs as the end result of a BBH collision. Like the inspiral of two black holes which is well understood with post-Newtonian theory, the ringdown of a black hole is well established by perturbation theory. The waveform depends on the internal parameters, the mass and spin of the final black hole, and its initial amplitude is set by the energy radiated during the merger. Echeverria [28] gave an analytic expression for the waveform assuming only the contributions of the dominant mode, $\ell = 2, m = 2$. Using this form, the ringdown waveform has been used in burst and inspiral searches [24, 40] as well as a model for both elucidating the Fisher matrix formalism for estimating the parameter errors due to instrument noise [29] and for different detection tiling algorithms [13, 40].

The Zerilli problem is a good model problem for the BBH waveforms since we can solve it numerically to generate waveforms for a large range of resolutions, a task that is computationally exhausting for the BBH case. The dominant source of error in the code is the truncation error, given by

$$w(t) = w_0(t) + c(t)\Delta r^p, \tag{2.1}$$

where $w_0(t)$ the the exact solution to the discrete equation, $c(t)\Delta r^p$ is the truncation error, Δr is the spatial grid spacing, p is the order of the truncation error and $c(t)$ is a time dependent scaling independent of the grid spacing. The truncation error will also be proportional to the square of the temporal spacing but this is dominated by the spatial step. The code we use is second-order accurate, $p = 2$, as shown in a convergence plot, fig. (2.1). Fig. (2.1) plots the scaled differences between the code output for five grid sizes, $\Delta r/m = (1, 1/2, 1/4, 1/8, 1/16)$ where m is the mass of the black hole and we use geometricized units where $G = c = 1$; and, therefore, the code units are transformed into seconds by multiplying by 5μ seconds per solar mass.

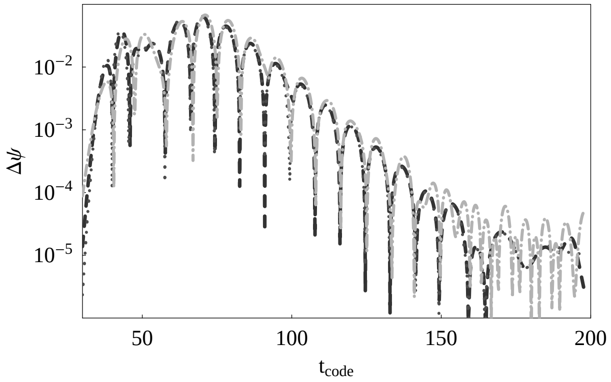

Fig. 2.1. There are three curves in this plot. They are $\psi(t, \Delta r = m) - \psi(t, \Delta r = m/2)$(gray, dot dashed), $4(\psi(t, \Delta r = m/4) - \psi(t, \Delta r = m/8))$(black, dotted), and $16(\psi(t, \Delta r = m/8) - \psi(t, \Delta r = m/16))$(black, dashed). This demonstrates second order convergence for the series of resolutions that we will be using in the analysis. The coarsest resolution shows larger percentage errors toward the end of the simulation as seen from the gray curve.

The gray line indicates the coarsest resolution used which has a larger error at the end of the simulation. The initial perturbation on the Schwarzschild background was given by an ingoing Gaussian pulse, $\psi(t=0,r) = e^{-(r-10m)^2/(3m)^2}$. We send in the dominant mode for a Schwarzschild black hole, the $\ell = 2$ mode. A typical ringdown waveform generated using the Zerilli code stretches over almost five orders of magnitude, about 8 e-folding times.

There are a couple of complications that arise when using ringdown templates. In order to isolate the ringdown from the initial pulse, we truncate the time series, ψ, at an appropriate time we call t_{cut}. This is similar to the problem of isolating the ringdown that Flanagan and Hughes point out [30, 31]. Here we use the Echeverria-Finn convention [28, 29, 21] and integrate over the $t > t_{cut}$ region ignoring $t < t_{cut}$. In the BBH waveforms, we may also choose to cut the waveform to remove the initial pulse contamination; however, that cut may be made at a low amplitude. In addition, the phase of the template is fixed by the initial data and, unlike the case for post-Newtonian templates, is not a free parameter that can be maximized over.

The output of the detector is the signal, $s(t)$, and it is related to the noise of the detector, $n(t)$, and the gravitational waveform, $h(t)$, such that $s(t) = n(t) + h(t)$. The scalar product between two functions $h_1(t)$ and $h_2(t)$ which are nonzero over some finite time duration T can be defined as

$$\langle h_1 | h_2 \rangle = \int_0^T h_1(t) h_2(t) dt, \tag{2.2}$$

where $||h|| \equiv \sqrt{\langle h|h\rangle}$. Note this definition is equivalent to the standard Fourier domain definition used in the literature

$$\langle h_1|h_2\rangle = 4Re\int_0^\infty \frac{\tilde{h}_1^*(f)\tilde{h}_2(f)}{S_h(f)}df,$$

for $S_h(f) = 1$, or white noise, by Parseval's identity. We chose to remain in the time domain to avoid the issues that arise in Fourier representation of ringdown signals[30] since these issues will not contribute to our understanding of the role of numerical errors in the analysis. We focus on the discretization of template parameters and chose no noise for simplicity which results in $s(t) = w(t)$. This leads to the absence of a mass scale: ie. the results of the overlaps scale with the total mass.

Just for this chapter, the template parameters are the mass m of the black holes and the numerical errors denoted by ϵ such that $\boldsymbol{\lambda} = [m, \epsilon]$ and $\boldsymbol{\mu} = \tau$, where τ is the time of arrival of the signal or the relative time lag between the signal and the template. When calculating the match, the maximization over τ is carried out for a template of arbitrary but fixed length smaller than the signal and, in practice, would be only as accurate as the smallest time step used numerically. We analyze the case of a family of templates provided by numerical relativity for detection that are given by $h^T(t; m_T, \epsilon)$, where T denotes the template. The templates are related to the exact waveform, $h(t, m)$ by

$$w(t; m_T, \epsilon) = w_0(t; m_T) + \epsilon\delta_\epsilon w(t; m_T), \tag{2.3}$$

where $\epsilon = \Delta r^2$ and $\delta_\epsilon w(t)$ is an error function that is independent of ϵ and equivalent to $c(t)$ in eqn.(2.1) but is renamed $\delta_\epsilon w(t)$ for notational convenience when we expand the match. This equation is just Richardson's ansatz [47], truncated to the leading order of our finite differencing scheme, which holds for any solution of a centered finite differencing approximation with a uniform mesh. We will further assume that the waveform that nature produces is represented by the solution, $h(t;m)$ such that $h(t) = w(t)$ and that the Zerilli function is the waveform template, $w(t, m_T, \epsilon) \equiv \psi(t, m_T, \epsilon)$.

2.2 Detection

2.2.1 The Match and Waveform Resolution

A statistic often used to compare templates is the normalized ambiguity function, also called the *match* (defined in eqn.(2.7) in [41] and in [27]). The match is a measure of how close a signal with given values of intrinsic parameters is to a template with different ones. We follow the notation of [41] and set $\boldsymbol{\lambda}$ to represent the intrinsic parameters like the mass of the black hole and $\boldsymbol{\mu}$ to represent the extrinsic parameters such as sky location and time of arrival that do not affect the dynamics of the waveform. The match between two waveforms of slightly different parameters, $h_1(t;\boldsymbol{\lambda}_1,\boldsymbol{\mu}_1)$ and $h_2(t;\boldsymbol{\lambda}_2,\boldsymbol{\mu}_2)$, is defined as

$$\mathcal{M}[h_1, h_2] \equiv \max_{\mu_1,\mu_2} \frac{\langle h_1(t;\boldsymbol{\lambda}_1,\boldsymbol{\mu}_1) | h_2(t;\boldsymbol{\lambda}_2,\boldsymbol{\mu}_2)\rangle}{||h_1(t;\boldsymbol{\lambda}_1,\boldsymbol{\mu}_1)||\ ||h_2(t;\boldsymbol{\lambda}_2,\boldsymbol{\mu}_2)||}. \tag{2.4}$$

Numerically computed waveforms will likely not have an analytic form in terms of their parameters, $\boldsymbol{\lambda}$. We can, however, qualitatively investigate how the templates vary with small changes in their parameters, ϵ and m, for the simple case of the ringdown templates. The match between a signal of a template, $w(t; m_T = m, \epsilon)$ and a signal of a slightly different mass, $w(t; m + dm)$ is given by

$$\begin{aligned} \mathcal{M}[h, w] &= \mathcal{M}(m, dm, \epsilon) \\ &= \max_{\tau} \frac{\langle w(t+\tau; m+dm) | w(t; m, \epsilon)\rangle}{||h(t+\tau; m+dm)|| \; ||w(t; m, \epsilon)||}. \end{aligned} \tag{2.5}$$

Let us express the full variation of the match given in eqn.(2.5) between a signal of mass parameter $m + dm$ and a template of parameters (m, ϵ) as a function of the small perturbations around $dm = 0$ and $\epsilon = 0$ up to third order accuracy. In order to do so, first we rewrite the template in terms of the signal using eqn.(2.3) and introduce the variable $\delta_m h$, where $\delta_m h = (h(t; m + dm) - h(t; m))/dm$. We find that

$$\begin{aligned} \mathcal{M} &= 1 - \epsilon^2 \Delta_{\epsilon\epsilon} - dm^2 \Delta_{mm} \\ &+ 2 dm \epsilon \Delta_{m\epsilon} \left(1 - \epsilon \frac{\langle \delta_\epsilon h | h \rangle}{\langle h | h \rangle} - dm \frac{\langle \delta_m h | h \rangle}{\langle h | h \rangle} \right), \end{aligned} \tag{2.6}$$

where the functions Δ_{ab} for a, b running over m, ϵ are given as

$$\Delta_{ab} = \frac{1}{2} \left(\frac{\langle \delta_a h | \delta_b h \rangle}{\langle h | h \rangle} - \frac{\langle \delta_a h | h \rangle \langle \delta_b h | h \rangle}{\langle h | h \rangle^2} \right), \tag{2.7}$$

and the notation $h \equiv h(t; m)$ was used for brevity. Note that the $\delta_a h$ terms correspond to the finite difference approximations to the partial derivative with respect to the parameter a, and the terms in the expansion cannot be analytically calculated.

We consider two cases for the dependence on the match with resolution of the waveforms, one where we keep the mass of the template fixed and one in which we allow it to vary. The mass of the template being set equal to the mass of the signal ($dm = 0$) results in a special case of the match in eqn. (2.7) called the faithfulness, $\mathcal{F}$, of the templates [27] and is given by

$$\mathcal{F} = 1 - \epsilon^2 \Delta_{\epsilon\epsilon}. \tag{2.8}$$

The faithfulness is used to measure the loss of signal-to-noise ratio due to numerical errors in a template by expressing the numerical error as a perturbation of the template, although we are not including the noise as part of the analysis. The faithfulness is related to the accuracy criterion of Flanagan and Hughes (eqn. (8.6) in [31]) by

$$\Delta_{FH} \equiv 1 - \mathcal{F}.$$

We shall see in the following sections how the various terms in the expansion can heuristically explain the variation of the numerically calculated match with the parameters of the various templates.

The templates are generated by solving the Zerilli equation for a series of resolutions $\Delta r/m = 2^{(i-10)/2}, i \in \{0, 2, ..10\}$.

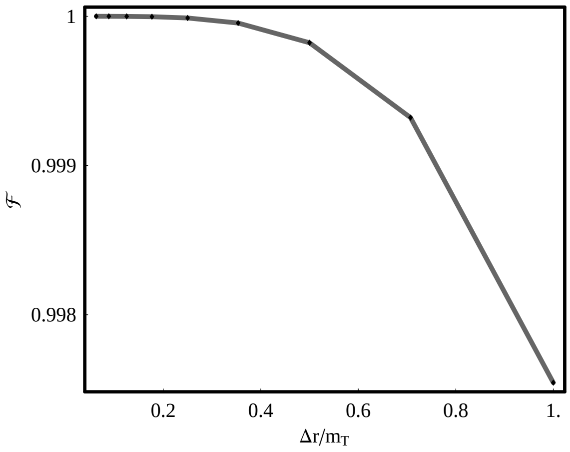

Fig. 2.2. The faithfulness, $\mathcal{F}$, decreases as the grid size increases. Note the actual values of $\mathcal{F}$ are very close to one, even for the coarsest resolutions of $\Delta r/m_T = 1$.

Fig. (2.2) plots $\mathcal{F}$ versus $\Delta r/m_T$. We see that the faithfulness decreases with increasing numerical error, as expected, but remains close to one even at the least resolved case. This verifies the recent findings of the BBH waveforms [53, 18]. The templates, w, are numerical and cannot be expanded around h analytically; however, the trend in the figure can be seen heuristically from eqn. (2.8), where we note that $\epsilon^2 = \Delta r^4$ as we have second order convergence. The term $\Delta_{\epsilon\epsilon}$ is the fractional loss of the signal to noise ratio due to the numerical error, defined by eqn. (2.7). For this Zerilli model, the numerical errors seem not to be a significant factor for detection if we only use the faithfulness statistic. The faithfulness, however, characterizes the behavior of the templates at just one point in the parameter space whereas quantities such as the match are defined in the neighborhood and more strongly reflect the presence of the numerical error as we see in the following subsection.

2.2.2 The Metric and the Template Space

In the previous subsection, we considered how the inefficiency of a single template in spanning the parameter space varies with resolution. The match gives the relative variation of the distance between points on the manifold, denoted by $\mathcal{M}[h, w]$. The template w and the signal h will, at best, lie on different manifolds that coincide as ϵ approaches zero, which assumes that the exact solution to the discrete equation represents nature's signal. Since we will not, in general, know the signal, we need a measure for laying down templates of various parameters on a grid in order to make a detection. This leads to a subcase of the match given by $1 - \mathcal{M}[w, w]$ known as the metric, $\mathcal{G}$ [41, 42]. The metric is a measure of the closeness of the templates of a given ϵ to each other and is written explicitly as

$$\mathcal{G} = 1 - \frac{\langle w(t; m + dm, \epsilon) | w(t; m, \epsilon) \rangle}{||w(t; m + dm, \epsilon)|| \; ||w(t; m, \epsilon)||}. \tag{2.9}$$

The metric is used to set up a template grid for detection and in §2.2.2 where we show how the difference between the $\mathcal{G}[w, w]$ and $\mathcal{M}[h, w]$ can lead to a loss in detected event rate.

The metric in the template space is specified by a minimum value for the fitting factor between the templates and the match if phase optimisation is ignored. First we evaluate $\mathcal{G}$, in the neighborhood of a template at a single resolution and then we will use

$\mathcal{G}$ to lay the next template at a different value of m. Since there is no intrinsic mass scale in the analysis, it is sufficient to lay two templates to tile the space. The generalization to N-templates is straight forward. When evaluating the metric, it is assumed that the signal is within the template manifold, i.e. $h = w$.

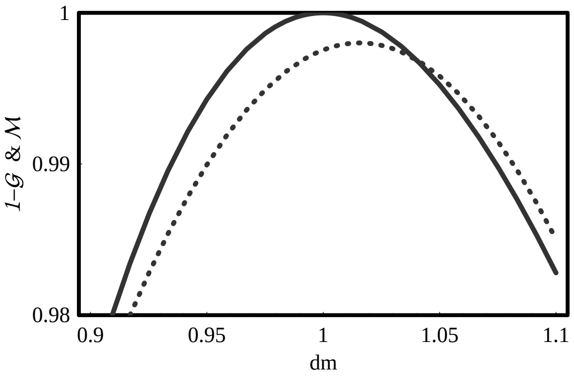

Fig. 2.3. The solid curve indicates the match $\mathcal{M}[w(t;m,\epsilon), w(t;m,\epsilon)] = 1 - \mathcal{G}$ of the templates of mass, m, with the base template of mass m=1. Both are constructed from the coarsest resolution $\Delta r/m = 1$. The dotted curve is the match of the base template with the signal $h(m)$. Note for high thresholds there is a difference between the two in terms of the tiling area. Also the peak match is significantly different from unity, indicating the less than perfect effectualness of the numerical base template.

Fig. (2.3) shows how $1 - \mathcal{G}$ and $\mathcal{M}$ vary with dm for the coarsest resolution, $\Delta r/m = 1$. The difference between $1 - \mathcal{G}$ and $\mathcal{M}$ will indicate potential loss in events due to the tiling. To understand fig. (2.3) qualitatively, we expand the expression for the metric in terms of dm and ϵ to second order as follows:

$$\mathcal{G} = dm^2\Big(\Delta_{mm} + 2\epsilon\Big(\Delta_{m\epsilon}\frac{\langle\partial_m h|h\rangle}{\langle h|h\rangle} - \frac{\langle h|\partial_m \delta_\epsilon h\rangle\langle h|h\rangle}{\langle h|h\rangle^2}\Big)\Big) \tag{2.10}$$

This equation is very similar to the expanded match between h and w, see eqn. (2.7). The term in eqn. (2.7) that is second order in ϵ and first order in dm does not appear here because both the templates lie in the same submanifold over which the metric is defined, and hence this is a "true" metric. In addition, $dm = 0$ is an extremum of eqn. (2.10) unlike for eqn. (2.7). The effects of the numerical error now occur at higher order as we can see in the coefficient of dm^2. The numerical error again tends to reduce the span or the width of the parabolas, thus requiring a greater number of templates at lower accuracy to span the area.

The solid curves in fig. (2.4) indicate the template placement for two templates, one of $m_1 = 1$ and the other $m_2 = 1.15$ such that for any template of mass, $m_1 \leq m \leq m_2$, $1 - \mathcal{G} \geq 0.99$. If we were to have a signal, $h(m)$, that signal would have a match with the two base templates given by the dotted curve. Because of the numerical errors in the templates, there is an unanticipated hole in the parameter space, given by the gray line in fig. (2.4), where $\mathcal{M} < 0.99$ and signals in the corresponding parameter range would not be detected.

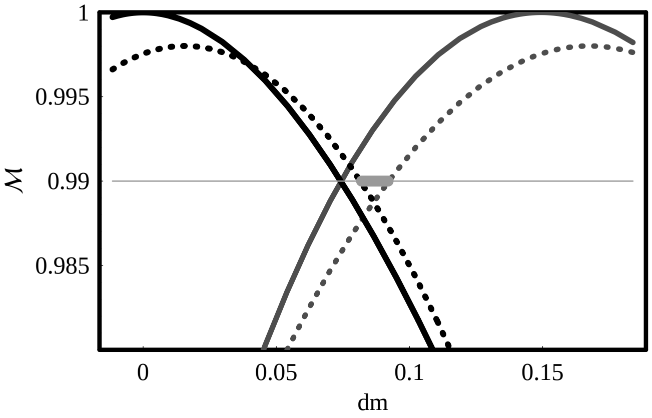

Fig. 2.4. The solid curves indicate the metric match between templates of the same numerical accuracy of $\Delta r/m_1 = 1$. The two solid curves are for different base templates, one for $m_1 = 1$ and one for $m_2 = 1.15$, chosen so that the threshold of 0.99 is crossed for all templates in between. The dotted curves indicate the match of these base templates with the exact signal h. In the highlighted region, $\mathcal{M}$ falls below the threshold and so the signals having their parameters in this region would not be detected. This leaves a hole in the signal parameter space spanned by the tiling not anticipated by the tiling scheme.

We plot the fraction of events missed by varying the threshold for two cases of low resolution, $\Delta r/m_1 = 1$ and 0.5 in fig. (2.5).

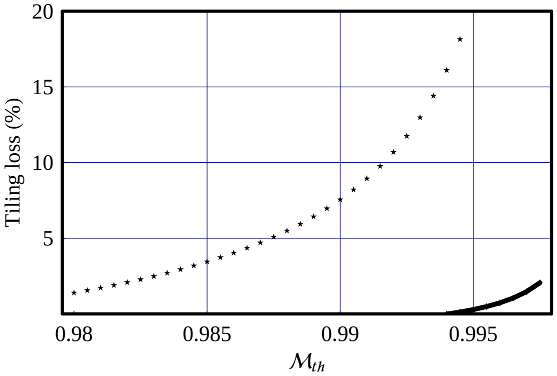

Fig. 2.5. The dotted line is the fraction of events missed by the template which tiles the parameter space without redundancy, for the coarsest resolution of $\Delta r/m_1 = 1$. For thresholds higher than 0.995, the loss increases monotonically up to 50% at a threshold of 0.9975, which is not shown here. For comparison, the solid line shows the loss for a more resolved case of $\Delta r/m_1 = 0.5$.

The fraction of events lost is purely due to the numerical error in the template. For every resolution, there is a critical threshold above which the holes will appear. This implies that the choice of the threshold determines the numerical accuracy needed.

In order to make a detection, we first need to create a template bank out of our Zerilli waveforms. In general, one would like to tile the parameter space for a given threshold with the minimum number of templates within an acceptable loss that will depend on the minimal match. When tiling a two-dimensional parameter space with templates, some events are lost, although the fractional loss will depend on the tiling scheme [13]. For the case of a one-dimensional parameter space, however, if the exact form of the signal is known, the tiling can be done without loss [48]. We find that some loss occurs even in a one-dimensional parameter space when tiled with templates containing numerical error.

The holes in the parameter space depend on the choice of tiling scheme. Avoiding the holes simply requires a tiling scheme that allows for overlapping spans of adjacent templates. For one-dimensional tiling this would not have been expected and arises from the fact that the errors cause the template not to lie on the signal manifold.

2.2.3 Efficiency of a Given Template in Spanning the Signal Parameters

The difference between the span of a low and high resolution template can be interpreted as the loss in the number of events due to its finite numerical accuracy assuming a uniform distribution of signal across the parameter space. This can also be called the *inefficiency*, χ, of the template. This inefficiency can be written as

$$\chi(\mathcal{M}_{th}, \epsilon) = 1 - Span(\mathcal{M}_{th}, \epsilon)/Span(\mathcal{M}_{th}, \epsilon = 0) \tag{2.11}$$

where $\mathcal{M}_{th}$ indicates a threshold match. The variation of the *Span* with ϵ is seen in fig. (2.8) for three values of $\mathcal{M}_{th}$. Fig. (2.6) plots the χ versus grid size for a series of match thresholds.

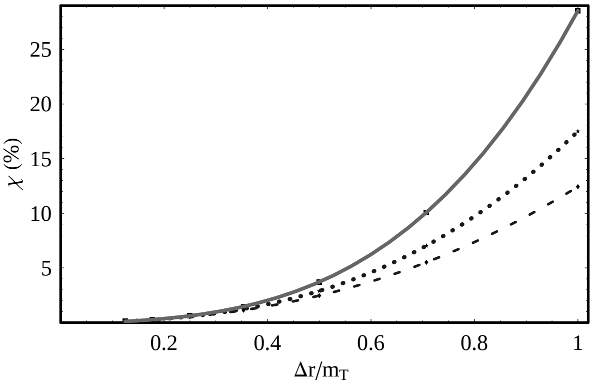

Fig. 2.6. The template inefficiency percentage in spanning the signal parameter space is plotted as a function of the grid size in the figure, for various thresholds. The solid line is for a threshold match of 0.995, dotted line for 0.99 and the dashed line for 0.98. The inefficiency increases as the resolution decreases or the threshold increases.

Fig. (2.6) indicates that for sufficiently fine grids the inefficiency is negligible; but for coarser grids and higher thresholds, the inefficiency is appreciably higher. Low resolution templates serve well for detection at low thresholds, but for high thresholds we may need more accurate templates. This conclusion will depend on the nature of the numerical errors of the true BBH waveform.

2.3 Mass Bias

Now we examine the match for a given set of templates and signal for variations of both variables, dm and ϵ. The templates span ϵ while their mass is kept fixed, $w(t, m_T = 1, \epsilon)$, and the signals span the mass, $h(t, m)$. First we explore the variation of $\mathcal{M}$ with $dm = (m - m_T)$ for different resolutions in fig. (2.7). Then we determine the variation of the detection thresholds with numerical errors using contours of the match in fig. (2.8).

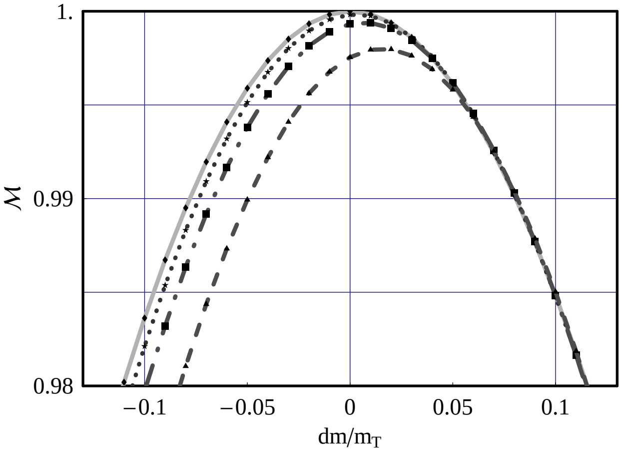

Fig. 2.7. The plot above shows the variation of the match $\mathcal{M}$ with dm/m_T (fractional mass difference between signal and template) for different grid sizes. The shift in the parabolas indicates event loss as well as the bias in the span over the mass parameter.

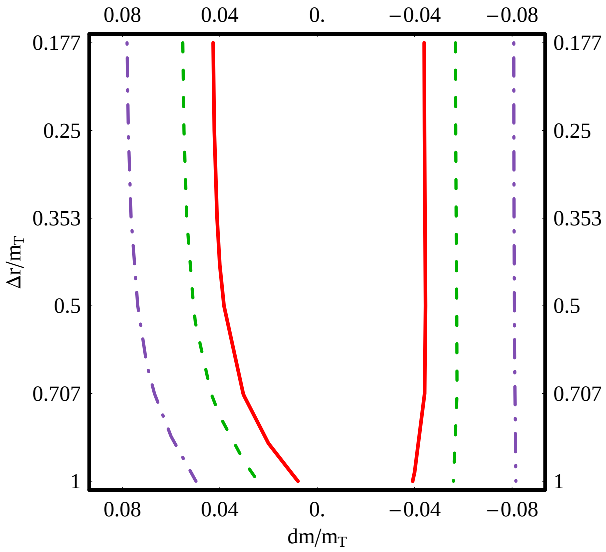

Fig. 2.8. The plot above shows the contours of the match with dm/m_T (fractional mass difference between signal and template) on x axis for different grid sizes (y axis). t=The contours are of match values from outside to inside 0.99, 0.995, and 0.997. The width of a contour of a certain match value denotes the *span* of the template in the signal space for that match threshold. In other words this is the signal parameter space covered by the template. The span decreases with resolution as you go down the y axis and the center of the span is biased away from zero due to the numerical error. This indicates that a low resolution template would be inefficient in detecting low frequency signals.

Fig. (2.7) shows that the variation of the match versus dm for various grid sizes, Δr, is almost parabolic. The shape of the curves is dominated by the dependence on dm and not as much on ϵ. There is an effect on the shape due to numerical errors, but this is only significant at high thresholds, which is seen more clearly in fig. (2.8). In fig. (2.8), the x-axis is m, the y-axis is Δr and the contours are of match values from outside to inside 0.99, 0.995, and 0.997. The span for a template at a given resolution and threshold value is the width of the corresponding contour. For example, for a template of grid size 0.25 and a match threshold of 0.99, the span is $1.08 < m < 0.92$. All the signals within that span will be detected for a threshold of 0.99.

The key features in the two plots are summarized in the following list.

- The peak of the parabolas move down as resolution decreases indicating a decrease in the maximum match achievable: the effectualness.
- The bias in the span is indicated by the drift in the parabolas of coarser resolution away from the base template. The base template is the the template in which $m = m_T = 1$. The contours show that this bias is more pronounced for higher thresholds than lower ones. The reduction in span can be interpreted as a fractional loss in the signal or inefficiency of the template in spanning the signal parameter space. We discuss this further in §2.2.2.
- The tendency of the parabolas to drift toward higher mass (lower frequency) causes an overall effect of numerical error to underestimate the mass (overestimate the frequency) of the signal.
- The width of the parabolas decrease slightly with decreasing resolution, the contour plot again indicates that this is more notably at high thresholds. This has implications for tiling, discussed in §2.2.2.

Although these graphs are constructed through numerical signals and templates, the bulk features can still be understood qualitatively using the functional form given in eqn.(2.7). The term in eqn. (2.7) that is bilinear in dm and ϵ causes the bias in span of the template while the presence of ϵ in the coefficient of the dm^2 term causes the reduction in the span for lower accuracy(higher ϵ) templates. The Δ_{mm} term in the coefficient of dm^2 is responsible for the near parabolic shape of the curves in fig. (2.7). The reduction and bias in the span causes some inefficiency in detection.

In the event of a detection one would want to extract the parameters of the source from the waveform. We evaluate the effectiveness of the templates in parameter estimation and the dependency on grid size. A measure of this effectiveness can be obtained by maximizing the match between a given signal and template by varying parameters. This measure is called effectualness [27] and is given by

$$\mathcal{E}(\epsilon) \equiv \max_{\eta} \mathcal{M}(\eta = m_T/m, \epsilon). \tag{2.12}$$

Note that we are now using templates of different mass and keeping the parameters of the signal fixed. The effectualness decreases with increasing grid spacing as seen in fig. (2.9).

The numerical error distorts the template space causing the template that gives the maximum match to have different parameters than that of the signal. The difference between the values of the parameters for the most effectual template and that of the signal is a systematic error, or bias, in estimating the parameters. Fig. (2.9) also shows that the parameter estimation biases can be significant (of the order of a percent) without significant effect on the effectualness.

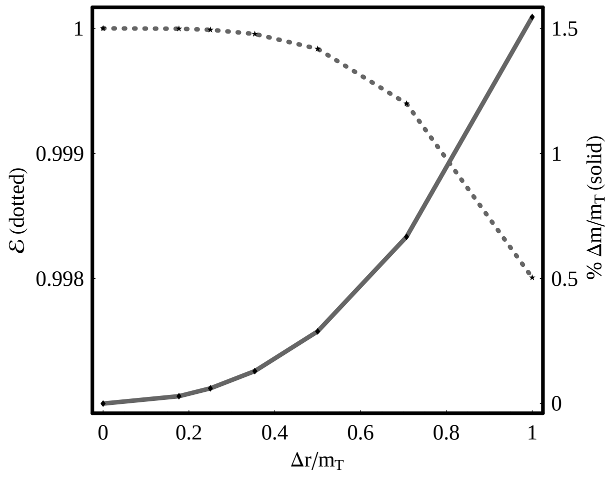

Fig. 2.9. The dotted curve indicates the variation of the effectualness with the grid size of the numerical simulation. The solid curve is the bias in the estimation of the mass in the signal due to the numerical error in the template. As the grid size increases, the effectualness of the template decreases and the bias in estimating the mass increases.

Effectualness is inversely proportional to the event loss. A larger effectualness implies that fewer events are missed in detection. As seen in fig. (2.9), the effectualness decreases with increasing grid size. This means that, for the coarsest resolution used, there can be a systematic bias of about 1.5% in estimating the mass of the black hole even *without* instrument noise.

2.4 Discussion and Directions

We study the effects of numerical error, namely the truncation error associated with finite differencing, on aspects of detection and characterization of the gravitational-wave signal. We generate black-hole ringdown templates numerically by solving the Zerilli equation. While the ringdown alone can be modeled by analytic fits, we use the numerical model to set the stage for future studies involving the necessarily numerical templates provided by numerical relativity for the BBH coalescence. These numerical Zerilli templates are analyzed for detection, tiling and parameter estimation using matched filtering.

The results of the paper are summarized as follows:

- Even for the coarsest resolution used in the study, the faithfulness $\mathcal{F}$ and effectualness $\mathcal{E}$ of the templates in detecting the signals are greater than 0.998. This suggests that, in this model, the numerical errors will not have significant impact on detection.

- We use the numerical templates to tile the parameter space such that no event would be lost if the templates were identical to the signal. Because of the numerical errors in the templates, the signal is not in the template manifold and we have unanticipated holes in the parameter space. For every resolution, there is a critical threshold above which the holes appear. These holes can be avoided by implementing a scheme that over-populates the tiling space.

- We find that the effect of numerical error is to induce a bias in the parameter estimation. This can be as great as 1.5% for the coarsest resolution. It is likely that this bias will carry over to the binary black hole case.

In this preliminary study, we have found that the mismatch and the bias induced by numerical errors is significant only for high thresholds. These numbers may be larger for the BBH merger waveforms for several reasons. In contrast to the BBH codes, the Zerilli code is one-dimensional and allows us to isolate the truncation errors. The largest grid sizes used in the Zerilli case are similar to those used in the BBH codes in the region where gravitational waves are extracted. We expect the trends discussed here to carry over to the BBH case; however, the phase errors will likely be more of a concern than truncation errors. This will also become more crucial as increasing numbers of orbits are computed. Future work will include the analysis for the BBH case and the inclusion of instrumental noise profiles.

Chapter 3

Formalism for data analysis of numerical waveforms

The aim of this chapter is to give an overview of the waveforms being studied as well as the mathematical formulae etc. which will be used for the calculations in further chapters.

3.1 The waveforms, numerical relativity considerations

The waveforms were extracted from the numerical evolution of the spacetime in terms of the Newman-Penrose scalar, $\Psi_4(t,x,y,z)$, which is expanded into angular modes via ${}_{-2}Y_{\ell m}(\theta,\phi)$, the spin-weighted spherical harmonics, by extraction on a sphere. The dominant mode for the quasi-circular orbits is the quadrupole mode ($\ell = 2$, $|m| = 2$). The angles θ and ϕ are given by the spin weighted $s = -2$, spherical harmonics, ${}_{-2}Y_{\ell m}(\theta,\phi)$, which correspond to the inclination and azimuthal angles between the source and detector in the source frame. Our waveforms are then parametrized by their total mass, the initial spins of the black holes, $a = J/M^2$, the angle of the spins with the orbit, ϑ and the inclination and azimuthal angles, θ and ϕ. We will only consider black holes of equal mass, $M_1 = M_2 = M$. When $\theta = 0$, the observer is directly above the orbital plane of the binary and sees primarily the $\ell = m = 2$ mode. As θ increases, the waveforms are a mixture of the non-zero modes which are all the modes we have extracted from the code, $\ell \leq 4$, except those modes that have zero amplitude within numerical error. Due to the trend of the spectral amplitudes we expect the higher order multiples to contain less than 1% of the signal. This will clearly change as more complicated waveforms are investigated than we study here.

3.1.1 The non precessing and precessing spinning waveforms

We study three sets of waveforms both the result of evolutions conducted by the PSU numerical relativity group. What we call the A-series was published in [33] and involves black holes of spins that are initially of equal-magnitude and anti-aligned, the spin axis is aligned with the axis of the orbital angular momentum. The initial black-hole spins covered the set $a = 0.0, 0.2, 0.4, 0.6, 0.8$.

The B-series was published in [34] and generalizes the A-series with variation of the initial angle, ϑ, at a fixed magnitude of spins, $a = 0.6$. When $\vartheta = 0$, we recover the A-series. When $\vartheta = \pi/2$, the spin-directions lie in the plane of the orbit and are in the"superkick" [32] configuration in which the maximum gravitational recoil from the BBH mergers has been found. In [34], it was found that despite the precession inherent in B-series, the black holes arrived at the plunge with the same entrance angle (see Fig.8 in [34]); and, therefore, in the cases we investigate, the initial and entrance angles are the same.

Since these waveforms were originally produced to study the gravitational recoil imparted to the final black hole after an asymmetric collision, only two to three orbits were evolved (the merger phase dominates the recoil). The number of orbits is set by the initial orbital frequency for a given total mass. In order to place the numerical waveforms firmly in the frequency band of the detector, we use the initial LIGO noise curve and we only investigate masses larger than $50M_\odot$ when calculating matches between waveforms. The total mass sets the frequency at which the signal enters the band. For example, the cutoff frequency for a binary system of $50M_\odot$ is $0.02/M$ or approximately 80Hz and about 40Hz for $100M_\odot$.

3.1.2 Non-spinning, eccentric binaries: the E-series

The waveforms from the E-series, start with initial data set to start the waveforms at much lower orbital frequency and the nearly zero eccentricity run in this case has nearly 16 cycles compared to the short waveforms for the spinning case. As a result one can take these waveforms as a realistic signal with the lower frequency cut off being at 40 Hz for initial LIGO, which is the case we are considering. The entire waveform is ”in-band” as a result.

It is important to keep in mind that the eccentricities we quote (and we use them also to label the models) are to be taken only as a guide to the eccentricity in the initial data, as the post-Newtonian (PN) expressions used do not include radiation reaction, and the PN parameters are in a different coordinate system to the puncture initial data. The initial eccentricity spans over $e = 0, 0.05, 0.1, 0.15, 0.2, 0.3, 0.4, 0.5, 0.6, 0.7, 0.8$.

The numerical simulations and results in this work were obtained with the same infrastructure used in our previous BBH studies (see Ref. [53] for full details). We have evolved the circular model at three different resolutions (finest grid spacings of $M/38.7$, $M/51.6$ and $M/64.5$). We obtain approximately fourth order convergence in the total energy and angular momentum radiated, consistent with the designed 4th order accuracy.

3.2 Data Analysis formulae

Our numerical waveforms are calculated during evolution in terms of the Newman-Penrose Ψ_4 at a radius of extraction r using

$$rm\Psi_4(t,\vec{r}) = \sum_{lm} {}_{-2}C_{lm}(t,r)\,{}_{-2}Y_{lm}(\theta,\phi)\,, \tag{3.1}$$

and r is the extraction radius. The relationship between Ψ_4 at future null infinity and the actual amplitude of the gravitational wave, $h(t)$, is given in terms of the two polarizations of the gravitational waves, $h_+(t)$ and $h_\times(t)$, as

$$\Psi_4(t) = \frac{d^2}{dt^2}(h_+(t) - ih_\times(t))\,, \tag{3.2}$$

which will be approximately correct due to the finite extraction radius. To carry out the matched filtering analysis, we compute the Fourier transform of the quantities $h_+(t)$ and $h_\times(t)$ called $\tilde{h}_+(f)$ and $\tilde{h}_\times(f)$ respectively. These transformed quantities are computed directly from the Fourier transform of the real part of Ψ_4 such that

$$\tilde{h}_+(f) = \mathcal{F}(\mathrm{Re}(\Psi_4))(f)/(-4\pi^2 f^2)\,. \tag{3.3}$$

This avoids issues regarding integration constants that arise from the time domain integration of Ψ_4 [20]. Our initial data contains gravitational radiation which does not correspond to that present in an astrophysical situation. This radiates away and is visible in the waveform as an *initial data pulse.* We remove this pulse from each waveform by removing the initial pulse from the time series of Ψ_4 where the pulse is distinct from the ramp up of gravitational wave amplitude. This does introduce a small error and ambiguity in where exactly to cut the waveform; however, the effect on the match of cutting off the initial data is smaller than the effect of the numerical error. Alternatively, leaving the initial data pulse in the waveform only adds noise to the spectrum and does not qualitatively change the results.

Our analysis of the match of the numerical relativity waveforms will follow along the lines of the matched filtering procedure for detecting gravitational waves. That is, given two time domain waveforms $h_1(t)$ and $h_2(t)$, the scalar or inner product between these two functions is defined as

$$\langle h_1 | h_2 \rangle = 4\,\mathrm{Re} \int_{f_{\min}}^{f_{\max}} \frac{\tilde{h}_1(f)\tilde{h}_2^*(f)}{S_h(f)}\, df, \tag{3.4}$$

where the domain $[f_{\min}, f_{\max}]$ is determined by the detector bandwidth and $\tilde{h}(f)$ stands for the Fourier transform of the respective time series. $S_h(f)$ denotes the noise spectrum for which we use the initial LIGO noise curve. The fact that our numerical waveforms only contain a few orbits before merger means that they do not span the entire LIGO frequency band. The initial orbital frequency of these runs varies depending on the value of the spin between approximately $0.016/m$ and $0.024/m$. The most stringent lower limit on $f_{\min}$ would be $0.024/m$. We impose the condition that the signal-to-noise ratio would be coming entirely from the domain spanned by our numerical waveforms such that $f_{\min}$ is calculated for each mass of the template. This fixes the lowest mass for which the templates could be useful to $50M_{\odot}$. The maximum signal-to-noise ratio ρ obtained in the case when the source and template waveforms match exactly, is given by

$$\rho = \left[4 \int_{f_{\min}}^{f_{\max}} \frac{|\tilde{h}(f)|^2}{S_h(f)} \right]^{1/2} . \tag{3.5}$$

The maximum signal-to-noise ratio ρ contained in each separate spherical harmonic mode of the waveform $h_{lm}(f)$, is given by

$$\rho = \left[4 \int_{f_{\min}}^{f_{\max}} \frac{|\tilde{h}_{lm}(f)|^2}{S_h(f)} \right]^{1/2} . \tag{3.6}$$

3.2.1 The phase optimized matches

The match statistic [41] measures the loss of the signal-to-noise ratio due to the template not being the same as the signal. It is properly defined as the overlap between the signal and the template maximized over all the intrinsic parameters, however, we will use it as a comparison measure between two templates h_1 and h_2. There are two extrinsic parameters: the time of arrival of the signal, t_0, and the initial phase of the orbit when it enters the LIGO band, Φ. First, consider the maximized overlap between templates defined with only maximization over time given by

$$O_{max}[h_1, h_2] \equiv \max_{t_0} O[h_1, h_2] \tag{3.7}$$

$$O[h_1, h_2] \equiv \frac{\langle h_1 | h_2 \rangle}{\sqrt{\langle h_1 | h_1 \rangle \langle h_2 | h_2 \rangle}} . \tag{3.8}$$

In Eq. (3.7), the maximization is to be understood as the maximum overlap between h_1 and h_2 obtained by shifting the template in time, i.e. $h(t) \rightarrow h(t+t_0)$ leading to the numerator being written in frequency domain as

$$\max_{t_0} \langle h_1 | h_2 \rangle = \max_{t_0} 4\mathrm{Re} \int_{f_{\min}}^{f_{\max}} \frac{\tilde{h}_1(f)\tilde{h}_2^*(f)e^{2\pi i f t_0}}{S_h(f)}\, df\,. \tag{3.9}$$

The Fourier transform is replaced by a discrete fast Fourier transform, transforming the integral into a discrete sum. When computing the match without phase optimization, we will typically compute the match of the templates using only h_+.

We also compute the match with an optimization over the phase, Φ of the template in addition to t_0. A waveform of arbitrary initial phase Φ is written as

$$\tilde{h}(f) = \tilde{h}_+(f)\cos\Phi + \tilde{h}_\times(f)\sin\Phi\,. \tag{3.10}$$

Given an arbitrary waveform, $\tilde{h}_1$, the phase optimization over the template, $\tilde{h}_2$, can be carried out using the normalized templates $e_{i,+,\times} = \tilde{h}_{i+,\times}/||\tilde{h}_{i+,\times}||$ where i runs over $1, 2$. In reference to the match we will always be referring to frequency domain templates and for ease of notation we shall refer to $\tilde{h}$ as h in the match formulae. The *typical* match [39] is given by

$$\begin{aligned} M_{\mathrm{typ}} &\equiv \max_{t_0} \max_{\Phi_2} O[h_{1+}, h_2] \\ &\approx \max_{t_0} \sqrt{O[e_{1+}, e_{2+}]^2 + O[e_{1+}, e_{2\times}]^2}\,, \end{aligned} \tag{3.11}$$

where we have assumed that e_{2+} and $e_{2\times}$ are nearly orthogonal, i.e. $\langle e_{2+}|e_{2\times}\rangle \approx 0$. This approximation is valid only for angles near ($\theta = 0$, $\phi = 0$) where the contribution from the modes other than $\ell = |m| = 2$ is negligible in comparison to the numerical errors. For a general waveform at nonzero θ and ϕ, the overlap of the corresponding h_+ and $h_\times$ is of the order of a few percent. In our spinning waveforms, we find a maximum deviation from orthogonality of $\sim 3\%$ at an angle that approaches $\pi/2$. In order to avoid uncertainties in the matches at large angles, we construct an orthonormal waveform basis as done by [49, 39] and outlined below.

Any arbitrary polarization other than $(+, \times)$ can be expressed as a linear combination of these linearly independent basis vectors. The phase optimization of the match can then be done in terms of the new orthonormal basis vectors, one of which we choose to be e_{i+} and the other $e_{i\perp}$ given as

$$e_{i\perp} = \left(e_{i\times} - e_{i+}\langle e_{i+}|e_{i\times}\rangle\right)\left(1 - \langle e_{i+}|e_{i\times}\rangle^2\right)^{-1/2}. \qquad (3.12)$$

One can see that $\langle e_{i+}|e_{i\perp}\rangle = 0$ by construction. Given such orthonormalized basis vectors for two sets of parameters $i = 1, 2$, we can calculate the upper and lower bounds on the phase optimized match [27].

In this new orthonormal basis, we rewrite the typical match from Eq. (3.11) by matching the + polarization of one template while optimizing over the phase of the other. This mimics the situation in which one of the waveforms acts as the template and can be maximized over its phase, Φ_2, while keeping the phase of the second template, Φ_1, fixed, as follows

$$\begin{aligned} M_{\rm typ} &\equiv \max_{t_0} \max_{\Phi_2} O[h_{1+}, h_2] \\ &= \max_{t_0} \sqrt{O[e_{1+}, e_{2+}]^2 + O[e_{1+}, e_{2\perp}]^2}\,. \end{aligned} \tag{3.13}$$

In general, the phase of the signal could take any value, and one would like to know the best and worst possible values of the match. The expression for the *best* match (the upper bound) is given by [27]

$$\begin{aligned} M_{\rm best} &\equiv \max_{t_0} \max_{\Phi_1} \max_{\Phi_2} O[h_1, h_2] \qquad (3.14) \\ &= \max_{t_0} \left[\frac{A+B}{2} + \left[\left(\frac{A-B}{2}\right)^2 + C^2\right]^{\frac{1}{2}}\right]^{\frac{1}{2}} \end{aligned}$$

in which the phases of each template are optimized. The *minimax* match is given by the case when one maximizes the phase of one of the templates but minimizes over the other. This is to mimic the worst case scenario when the signal phase is such that it gives lower matches even when maximized over the template phase, given by [27]

$$\begin{aligned} M_{\rm minimax} &\equiv \max_{t_0} \min_{\Phi_2} \max_{\Phi_1} O[h_1, h_2] \qquad (3.15) \\ &= \max_{t_0} \left[\frac{A+B}{2} - \left[\left(\frac{A-B}{2}\right)^2 + C^2\right]^{\frac{1}{2}}\right]^{\frac{1}{2}} \end{aligned}$$

and for both cases the functionals A, B, C are written in terms of the ortho-normal basis functions $(e_{1+}, e_{1\perp})$ and $(e_{2+}, e_{2\perp})$ corresponding to the two templates being compared

$$
\begin{aligned}
A &\equiv \langle e_{1+} | e_{2+} \rangle^2 + \langle e_{1+} | e_{2\perp} \rangle^2 , \\
B &\equiv \langle e_{1\perp} | e_{2+} \rangle^2 + \langle e_{1\perp} | e_{2\perp} \rangle^2 , \\
C &\equiv \langle e_{1+} | e_{2+} \rangle \langle e_{1\perp} | e_{2+} \rangle + \langle e_{1+} | e_{2\perp} \rangle \langle e_{1\perp} | e_{2\perp} \rangle .
\end{aligned}
$$

Note the symmetry of the formulae upon interchange of the two templates which arises from the fact that only the *relative phase* between the two templates should matter. Because of this, which template is maximized and which minimized is interchangeable. We will refer to the target's phase being minimized and the template's phase being maximized since this makes sense in a detection scenario.

3.2.2 Faithfulness and Fitting Factor

A measure for the loss of signal-to-noise first used by [3] consists in maximizing over all the intrinsic and extrinsic source parameters. Since we do not have control of the initial phase of the signal, we would like to accommodate the worst case scenario by considering a minimax type of quantity, which is at the same time maximized over the mass of the quasi-circular non-spinning template for example. Thus we shall use a slightly different definition of the fitting factor than [39, 11]. For a signal waveform $s(m)$from a binary with total mass m, and a template $h^T(m_T)$ of mass parameter m_T, the fitting factor is defined as

$$FF \equiv max_{m_T} min_{\phi_s} max_{t_0,\phi_h} O[s(m), h^T(m_T)] \tag{3.16}$$

We shall use this definition while considering the eccentric binary black hole signal detection in chapter six.

A special case of the matches arises when all or some of the intrinsic source parameters of the two waveforms being compared are identical. For example in comparing a spinning and a non-spinning waveform or an eccentric and a circular waveform, one could keep the mass identical for the two. In this case we shall use the term faithfulness to mean the minimax match, wherein the mass parameter of the two waveforms is identical.

Chapter 4

The impact of finite differencing errors on matches

Both numerical accuracy, e.g. truncation errors, and astrophysical accuracy, e.g. initial data choices, will play a role in determining the viability of numerical relativity BBH waveforms acting as templates. Requirements may be more stringent when characterizing the sources of gravitational waves; however, in this chapter we focus on the use of numerical relativity waveforms as potential templates for detection, not for parameter estimation.

4.1 The accuracy of quasi-circular merger waveforms

Requirements for detection were first placed on waveforms from BBHs generated by numerical relativity in references [30, 31]. This early work preceded the successful solution of the BBH problem by many years, but acts as a guide for determining the constraint on numerical resolution accurate enough for data analysis purposes. These methods were used by Miller [37] to establish accuracy requirements for parameter estimation in a neutron star binary situation. A similar method was employed more recently in reference [18] in connection with BBH evolutions of equal-mass, non-spinning black holes over several orbits. Ref. [18], made a prediction of a maximum match that numerical waveforms will resolve. In addition, we did a preliminary study of the impact that numerical errors can have on the faithfulness of numerical waveforms using a Zerilli-based toy model in [54]. We now employ similar tests as [30] and [18] and verify the predicted behavior of the match with resolution for our BBH evolutions. The dominant mode in the waveform at an arbitrary inclination in source frame, in the inspiral case is the quadrupole mode ($\ell = 2$, $|m| = 2$). For compact binary inspiral searches, restricted post-Newtonian templates are commonly used for detection [26]. These templates include only the dominant harmonic in the amplitude while including as much information as possible in the phase since phasing is the more important issue in matched filtering. Corrected-amplitude templates have been considered in [56] and found to reduce the signal-to-noise ratios for LIGO and add features to the detection and parameter estimation for Advanced LIGO [57, 58].

In [18], it was found that using the $\ell = 2$ mode was good enough for detecting gravitational waves of non-spinning, equal mass binaries in quasicircular orbits. We include in our analysis the angle from the spherical harmonics, θ and ϕ, where θ is related to the inclination angle of the binary with respect to the detector but in the source frame. The waveform at a given angle is reconstructed from the different spin-2 spherical harmonic modes (ℓ, m) using modes $\ell \leq 4$, the higher modes are too small to resolve over numerical error. We find that, in general, we will need to include modes other than the dominant $\ell = m = 2$ to accurately represent spinning BBH waveforms. We also explore the sensitivity of the match with the spin parameter of the black-holes' initial angular momentum and how well a reduced template bank would do in matching with a target template of arbitrary spin and inclination.

We present our results for the variation of the match with resolution, including convergence tests of the waveforms in the mass range of $50M_{\odot}$ to $300M_{\odot}$. The spectra of the BBH waveforms from the models R1 and S0.05-S0.20 are shown in Fig. 4.1, in which we plot $|h(f)|$. The $\theta = 0$ lines correspond to the $\ell = |m| = 2$ mode. The final black hole in all these runs settled to the same final spin with a spin parameter $a \approx 0.66$.

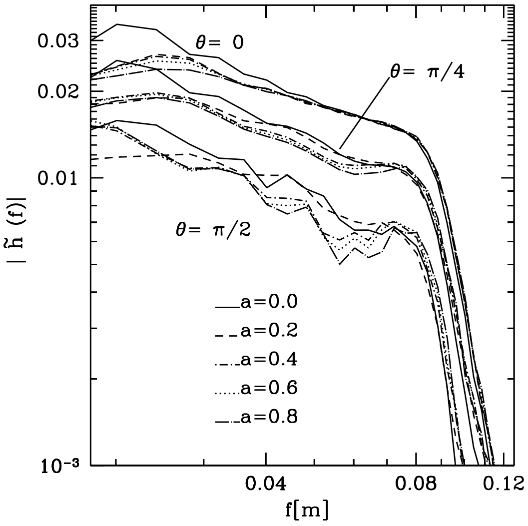

Fig. 4.1. The spectrum of the wave versus frequency of waveforms from different initial spins in a log-log plot.

In Fig. 4.1, when $\theta = 0$, the spectra for each value of a become very similar for $f > 0.05m$. This is because all of the configurations we evolved settled down to very similar final black holes. The spinning cases all have resolutions of $m/40$ and the non-spinning, $m/38.4$. We present three cases of inclination angle, θ, for each set of spins, and the units are $f_{\text{code}} = f_{\text{phys}}/m$. When θ deviates from zero, however, the spectra show that there is significant variation between the different spinning waveforms. This is in part due to the larger resolution requirements for the higher harmonics, however, as we shall see in the following results, the resolution differences do not account for all of the variation.

Firstly, in §4.2, we investigate the convergence of the dominant, $\ell = |m| = 2$, mode for non-spinning BBHs, the convergence of the spinning waveforms was published in [33] to be between third and fourth order. In §4.3 we investigate the quality of the numerical waveforms as templates in matched filtering in terms of the resolution including spin and inclination angle. Next, in §5.3, we show how the inclusion of modes $\ell < 5$ affects the match calculations when compared to just using the dominant mode waveform $\ell = |m| = 2$ as a function of the spin. Additionally, we determine the effect of using a finite extraction radius on the quality of the matches. Lastly, in §7.2, we compare the different spin waveforms to each other, including the dependence on θ but keep the masses the same. This is equivalent to checking the *faithfulness* [27] of the waveforms assuming the orientation of the source for the different sources to be the same. While this assumption will need to be relaxed in a fully general treatment for data analysis, it suffices to demonstrate the importance and impact of using higher than dominant modes in the analysis of these merger waveforms.

4.2 Numerical Convergence

For simple linear systems such as the wave equation, it can be proved mathematically that a suitable finite differencing scheme to numerically solve the equation can yield solutions converging toward the continuum one as the numerical grid size is refined. For the nonlinear Einstein equations, this sort of mathematical proof is not possible. We instead show results from several simulations and assess their consistency with fourth order convergence. A convergence test of the spinning series of runs called S0.05-S0.20 is given in [33]. Here we investigate the quality of our numerical waveforms with a convergence test of the equal-mass, non-spinning R1 series of runs. These runs are named R1a-R1f and only differ in their resolution. The suffix corresponds to the grid spacing of the finest grid surrounding each black hole. The grid spacings are $\Delta_{a-f} = \{M/25, M/32, M/38.4, M/44.8, M/51.2, M/57.6\}$. We consider the convergence properties of the $\ell = m = 2$ mode of Ψ_4 computed on the coordinate sphere at $r = 30$. In Fig. 4.3 we plot $\mathrm{Re}[\Psi_4^{2,2}]$, and Fig. 4.2 shows that $\Psi_4^{2,2}$ computed at $r = 30$ appears to converge monotonically with resolution to a continuum solution, and that the high resolution results agree well with each other. Similar results (not shown) are obtained for $\arg \Psi_4^{2,2}$ and the coordinate locations of the black holes. Using the runs R1a, R1b, and R1f we demonstrate fourth order convergence of the amplitude and phase of $\Psi_4^{2,2}$ in Fig. 4.4 and Fig. 4.5. Note that if the resolutions being compared are very close to each other, the difference between, say, fourth and fifth order convergence in Fig. 4.4 is small, so we explicitly show how the curves should overlay for third, fourth and fifth order, and show that the results are more consistent with fourth order than third or fifth. If we plot only the highest resolution runs, we find that the fourth order convergence is lost; i.e. there is a source of error which spoils the convergence at high resolutions. However, as can be seen from Fig. 4.2, the waveforms still appear to converge to a continuum solution, just at a different order.

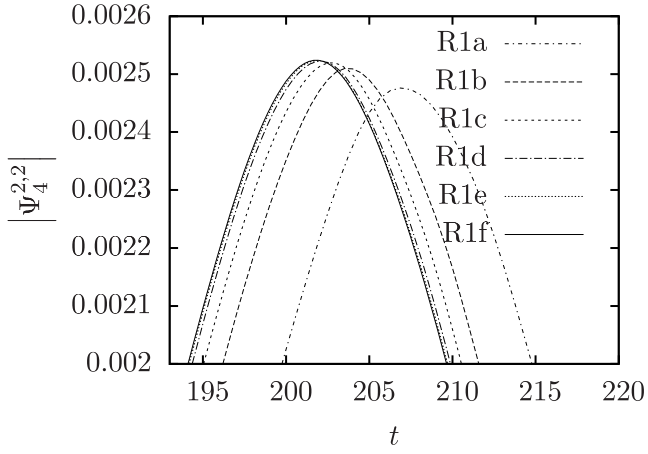

Fig. 4.2. Monotonic change in $|\Psi_4^{2,2}|$ as resolution is increased. It appears that the function is converging to a continuum solution.

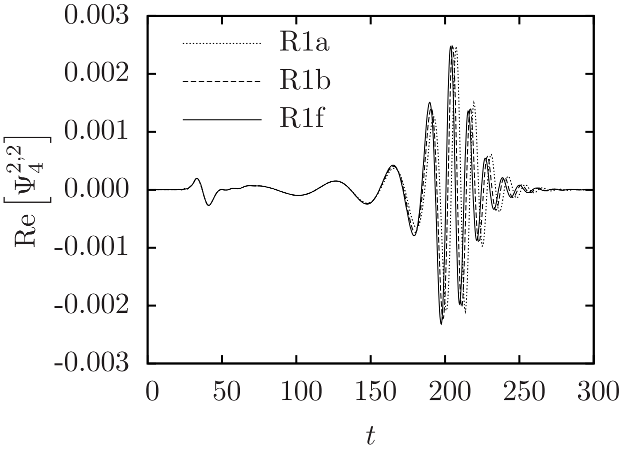

Fig. 4.3. $\mathrm{Re}[\Psi_4^{2,2}]$ computed at $r = 30$ for three different resolutions. The feature at $t = 40$ is due to the gravitational radiation present in the initial data, and will be cut out of the waveform before taking Fourier transforms for data analysis.

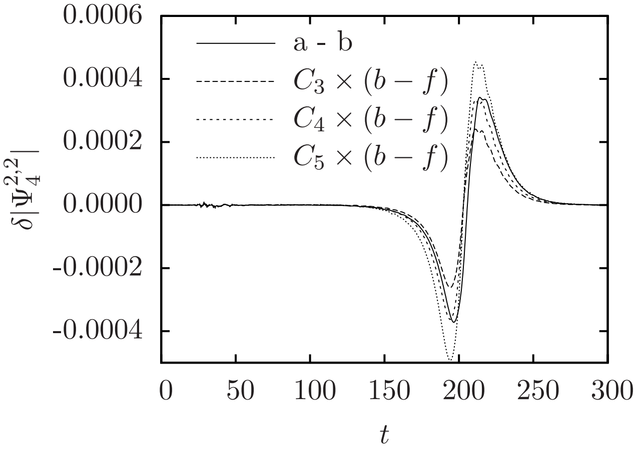

Fig. 4.4. Convergence of $|\Psi_4^{2,2}|$ using the highest and the two lowest resolutions. C_3, C_4, C_5 are the scaling factors expected for third, fourth and fifth order convergence respectively. We see that $a - b$ matches most closely with $C_4 \times (b - f)$ indicating fourth order convergence.

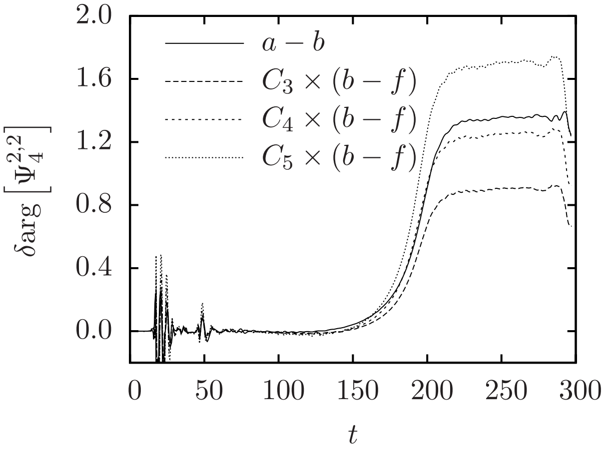

Fig. 4.5. Convergence of arg $\Psi_4^{2,2}$. As in Fig. 4.4, we see fourth order convergence.

4.3 Variation of Templates with Resolution

We can follow the numerical convergence properties through matched filtering since we know how the numerical codes approximate the exact solution to the partial differential equations discretely. For finite differencing this is expressed as

$$h(t) = h_0(t) + c(t)\Delta^p + \mathcal{O}(\Delta^{p+1}) \tag{4.1}$$

where $h_0(t)$ is the exact solution found when the resolution goes to infinity, Δ is the grid spacing ($\Delta = \Delta x = \Delta y = \Delta z \propto \Delta t$), p is the order of the truncation error and $c(t)$ is a time dependent scaling independent of the grid spacing. Since our code is approximately fourth order accurate, we expect to scale with $p = 4$. One can calculate $h_0(t)$ using Richardson extrapolation of three discrete, convergent solutions of different resolution.

We have computed $h_0(t)$ for the R1 series of runs using R1a, R1b, and R1f and found that $h_0(t)$ coincides to within 10^{-5} in amplitude with the waveform evolved with the finest resolution, $\Delta_f = M/57.6$. In light of this, we will use our finest resolution run, indicated as $h(\Delta_f)$, in place of the Fourier transform of $h_0(t)$.

We can predict the behavior of the maximized overlap as a function of resolution between two waveforms that differ only in their resolution by expanding the match equation, Eq.(3.7), about $\Delta^p = 0$. Note that when Δ^p is a constant in time, we can express Eq.(4.1), in the Fourier space as $h_i = h_0 + c\Delta^p_i$, where i labels each waveform. We expand the match for the case of two templates at two different resolutions to be as general as possible, i.e. $O[h_1(\Delta_i), h_2(\Delta_j)]$ as follows

$$\begin{aligned} O[h_i, h_j] &= 1 - \frac{1}{2}(\Delta^p_i - \Delta^p_j)^2 \left(\frac{\langle c|c\rangle}{\langle h_0|h_0\rangle} - \left(\frac{\langle c|h_0\rangle^2}{\langle h_0|h_0\rangle^2} \right) \right) \\ &+ \mathcal{O}^{(3)}(\Delta^p)\,. \end{aligned} \tag{4.2}$$

The above equation was expanded for two matches of different resolution but the match with the Richardson extrapolated solution can be recovered by setting $\Delta_j = 0$ up to the order expressed. This equation indicates that the mismatch, $(1 - O_{\max})$, goes like Δ^{2p}. Fig. (4.6) shows the dependence of the $O_{\max}$ on the resolution for three choices of the total mass, $m = \{50, 100, 200\}M_\odot$. The least squares fit is done for several possible values of Δ^{2p} including $p = 3, 4, 5$. The best fit is found for $p = 4$, and is the fit pictured in Fig.(4.6).

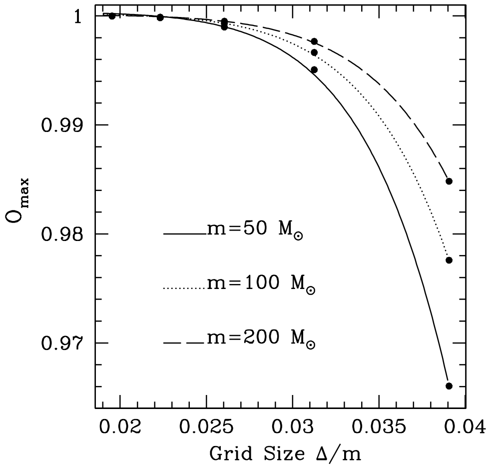

Fig. 4.6. The maximized overlap, $O_{\max}[h_i, h_f]$, from Eq. (3.7) is plotted as a function of grid size for three total masses indicating fourth order convergence. The data are given by the points and the least square fitting by the lines. The $p = 4$ fit differs for different masses because of the weighting by the current LIGO noise curve $S_h(f)$.

Because of the computational cost of generating solutions to the Einstein equations at three resolutions for every waveform of interest, Flanagan and Hughes [31] suggested computing the match between templates of neighboring resolutions, such as $O_{\max}[h(\Delta_a), h(\Delta_b)]$ for example. A variation, used by Baumgarte et al [18], is to compute the series of matches as $O_{\max}[h(\Delta_i), h(\Delta_f)]$, where the first template runs over all the resolutions available, denoted by Δ_i, and the second template's resolution is fixed to the finest available.

We plot the Flanagan and Hughes type of overlaps, $O_{\max}[h_+(\Delta_a), h_+(\Delta_b)]$ and $O_{\max}[h_+(\Delta_b), h_+(\Delta_c)]$ and three cases where we vary the resolution of one template while keeping the second template fixed to the finest resolution, $O_{\max}[h_+(\Delta_i), h_+(\Delta_f)]$ where $i = a, b, c$, in Fig. (4.7). These matches are unoptimized over the phase, but optimized over the time t_0 and follow the definition given in Eq. (3.7).

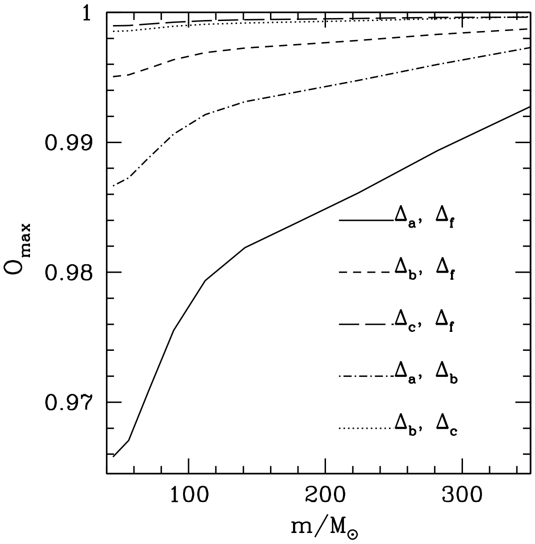

Fig. 4.7. The maximized overlaps, $O_{\max}[h_{1+}, h_{2+}]$, are plotted as a function of mass for several resolutions of our equal-mass BBH series of runs. Labels (a, b, c) stand for the coarse runs $R1a, b, c$ with resolutions $m/25.6$, $m/32.0$, $m/38.4$, while $R1f$ has resolution $m/57.6$. The overlap between adjacent resolutions $O_{\max}[h_+(\Delta_a), h_+(\Delta_b)$ has deceptively high values compared to the matches with the finest resolution.

The threshold of match above which the resolutions will be "good enough" for detection is typically set to 0.98. Clearly from the figure we can conclude for the $\theta = 0$, a resolution of $\Delta_b = M/32.0$ was enough for the entire mass range to reach a minimum match of 0.98 and that, for a lower resolution of $\Delta_a = M/25.6$, we only achieved $O_{\mathrm{max}} > 0.98$ for total masses larger than $100 M_\odot$. One of the main features of the matches with resolution is the decrease in the match toward smaller masses. This is partly due to the low number of gravitational wave cycles we have present in the waveforms. The numerical errors, however, will increase as we increase the total number of cycles so the choice of resolution will depend on the number of orbits evolved and details of the numerical scheme. As we evolve more cycles, we will also be extending the total mass range into smaller masses.

The matches are expected to get closer to one when phase optimization is included. Since the phase of a given signal waveform depends on the detector orientation and several such variables, it could differ from the template up to a constant phase factor and the match would vary depending on what the phase is. The worst case would occur when the arbitrary phase is such that there is maximum destructive interference between the target and the template, and sets up the lower bound on the possible matches, M_{minimax}. If one does not add any phase factor to the numerically generated template , one gets what is called the typical match and if the phase factor is chosen for maximum constructive interference, it yields the "best" match, M_{best}. The value of M_{best} is a measure of the closest distance between two templates. We'll use the minimax match for the rest of the paper to report our results in terms of lower bounds and use the typical and best matches to illustrate the range over the different type of matches.

To demonstrate the differences in the match with choice of optimization, we tabulate examples of optimization in Tab. 4.1 for few selected total masses between the coarsest and finest runs. No optimization at all is listed in the second column, optimization over just t_0 from Eq. (3.7) in the third, the typical match Eq. (3.13) in the fourth, minimax, Eq. (3.16), in the fifth and finally best match, Eq. (3.15), in the final column. The phase optimized matches, the last three columns, exceed the the threshold of $O_{\rm max} > 0.98$ for even the least resolved waveform when matched with the finest resolution waveform.

Table 4.1. Comparing matches with different optimizations between the coarsest ($R1a$) and the finest ($R1f$) runs for selected total masses. The second column is the normalized overlap between the two waveforms without optimization over t_0, the third column is the match with optimization over t_0, the fourth is the typical match, the fifth the minimax, and the final column is the best match.

m	O	$O_{\rm max}$	$M_{\rm typ}$	$M_{\rm minimax}$	$M_{\rm best}$
44.67	0.7987	0.9658	0.9979	0.9974	0.9983
70.79	0.5458	0.9709	0.9989	0.9989	0.9991
112.2	0.2308	0.9794	0.9994	0.9993	0.9995
177.8	0.04864	0.9837	0.9994	0.9993	0.9996
281.8	−0.06719	0.9893	0.9993	0.9993	0.9996

We also calculated the minimax matches, see Eq. (3.16), for all the $R1$ resolutions, although we do not plot them here, and found that for all the resolutions $M_{\rm minimax} \geq 0.99$ in the mass range under consideration and show the same variation as the overlap. These results hold only for $\theta = 0$ and $a = 0$.

We now analyze the resolution needs of the spinning BBH waveforms of which we only have three resolutions for each of the spinning configurations in contrast to the five available for the non-spinning case. These are labeled $\Delta_{\text{coarse}} = M/32$, $\Delta_{\text{med}} = M/38.4$, and $\Delta_{\text{fine}} = M/40$. Later in this paper, we find that it is necessary to include the higher modes for the spinning BBH templates; and, therefore, as we analyze the spinning BBH waveforms versus resolution we also include its variation with θ. At inclination angle $\theta = 0$ only the $\ell = |m| = 2$ mode is present in h, and when $\theta \neq 0$ all the modes get mixed. We do not include modes $\ell \geq 5$ in constructing h because these were too small to be well resolved for the evolutions we use in this paper. The variation of θ is presented for two suggestive cases, $\theta = \pi/4$ and $\theta \sim \pi/2$. Values of θ are not taken to be exactly on the plane since the radiation is then linearly polarized and cannot be described with two basis vectors and cannot be maximized over the phase at that point, but instead at $\theta = 89\pi/180$.

For the $\theta = 0$ case, all the spinning waveforms have a $M_{\text{minimax}} \geq 0.99$ over the entire mass range for matches between the Δ_{coarse} and Δ_{fine} and between Δ_{med} and Δ_{fine}. These matches also follow the same trend with mass, i.e. decreasing matches with decreasing total mass, as reported in Tab. 4.1. For $\theta \neq 0$, we plot the minimax match for the $a = 0.8$ spin case between both the highest and coarsest and highest and medium resolved waveforms at the two values of θ in Fig. 4.8. We only show the $a = 0.8$ waveforms since the matches of the high and low resolution of the other spin and non-spinning runs are all $M_{\text{minimax}} \geq 0.99$ at these angles again over the entire mass range. Note, however, that even though the matches are very high, they decrease with increasing spin. This is expected since we are keeping the number of points across the black hole fixed, but as the spin increases, the horizon area decreases, hence the effective numerical resolution of a high initial spin waveform is lower than that of a low initial spin waveform. The case of $\theta \sim \pi/2$ gave us the lowest matches of any angles between 0 and $\pi/2$ and shows that the minimax match of the Δ_{fine} and Δ_{med} resolutions is $M_{\text{minimax}} \geq 0.97$. While the match of the coarsest resolution run at higher masses is $M_{\text{minimax}} \sim 0.92$, which indicates that the coarse resolution is not good enough for meeting the threshold when $a = 0.8$ and $\theta \sim \pi/2$. For the rest of the paper, we will use the finest resolution for all spin cases to ensure that the errors due to resolution are no greater 3% in the most difficult case to resolve: the high spin, high angle case, and should be much lesser in other cases.

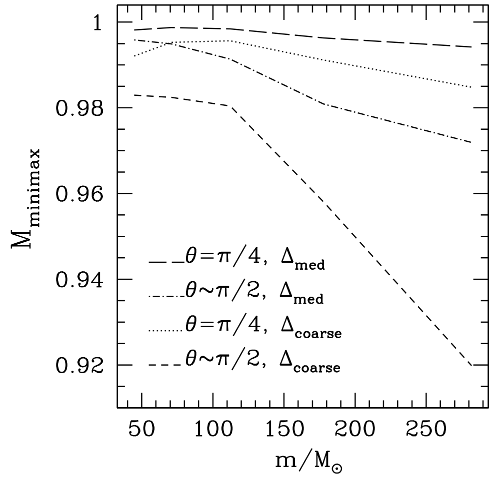

Fig. 4.8. We plot the minimax match between the waveforms of $a = 0.8$ for two cases of inclination angle, $\theta = \pi/4$ and $\theta = \pi/2$ and two different resolutions $\Delta_{\rm fine}$ with $\Delta_{\rm med}$ and $\Delta_{\rm fine}$ with $\Delta_{\rm coarse}$. Corresponding matches for lower spins are all ≥ 0.99 and are not shown here.

Fig. 4.8 shows two features of the minimax match, namely it decreases with increasing θ and with increasing mass. The decrease of the match in Fig. 4.8 at higher mass is in contrast to Fig. 4.7. There are two differences between the figures, one is the phase optimization which, from Tab. 4.1, we can see does not change the trend of the match versus mass. The second difference is the inclusion of higher modes. The overall match will be reduced with non-zero θ since the frequencies of the modes increase with ℓ, placing stronger resolution requirements. The highest spin we analyze, $a = 0.8$, has the lowest minimax matches of all the spin cases, as low as $M_{\rm minimax} = 0.92$ at the largest angle. Large spins demand more resolution in general and this is seen particularly when resolving modes with $\ell > 2$. For the lower spin runs, $a \leq 0.6$, the waveforms are well resolved and the matches are all ≥ 0.99 over the entire mass range even for $\theta \sim \pi/2$. The decrease in match is seen most strongly at the larger mass range since this mass range targets the merger and ringdown part of the signal. We expect these match values and all the matches reported in this section to change for waveforms with more gravitational wave cycles since the numerical errors will grow as the length of the run increases and the accumulating phase errors will likely play a larger role.

4.4 Are the waveforms good enough for detection?

The issue of how good the waveforms need to be for detection depends also on how close these numerical relativity evolutions are to the waveforms from nature. One objection that can be raised is that the numerical relativity initial data is conformally flat and hence the waveforms may not match the physical ones. The resolution to this objection would be if one could evolve the waveforms from far enough separation that they could be compared to the post-Newtonian ones and also assess the validity of the different approximation schemes in the late inspiral regime.

Such studies are now available, indicating that for atleast the equal mass, non-spinning binaries, the waveforms can be matched to the post-newtonian ones at sufficient far separations, to within suitable error bars in amplitude and phase [6]. How this matching carries across the parameter space of spinning and unequal mass systems will become evident as more such comparisons are performed. The issue relevant for numerical relativist would then be, do they have to stick to the highest accuracy afforded in order to start contributing to gravitational wave detection or is it possible to contribute via several low resolution runs spanning a bigger parameter space?

Given the numerical convergence properties of our waveforms, we first predict and show that the match has a dependence on the resolution of Δ^{2p}, in which a fourth order evolution scheme has $p = 4$. For the resolutions of our BBH evolutions, we get very high matches (> 0.98) for resolutions above $M/32$ when $a = 0$ and above $M/38$ for waveforms with $a = 0.8$. The resolutions are only appropriate for the cases we have investigated. For the waveforms generated out of the $\ell = |m| = 2$ mode, we find that the match values between the same waveforms at different resolution decreases as the total mass decreases. We only report matches from $50M_{\odot} - 300M_{\odot}$, where $50M_{\odot}$ is set by our initial orbital velocity.

While the question remains an interesting one, the indications are that moderate amount of finite differencing errors in numerical relativity runs are not a handicap to their applicability to detection, for the larger mass scales, the resolution increase is important as the higher modes, which are more difficult to resolve, play an increasing part. The resolution will also be very important in parameter estimation, and a low resolution merger waveform will lead to biases in the inferred physical parameters.

Chapter 5

Higher multipole modes in spinning binary black holes

5.1 The waveform for a detector at an arbitrary inclination

The multipolar analysis of BBH waveforms produced by numerical relativity has been pursued for both unequal mass and spinning BBH configurations [50, 20, 19]. Using only the dominant mode in comparing waveforms, tantamount to choosing an inclination angle with the detector in the source frame of $\theta = 0$, results in a degeneracy of the A-series parameter space for example.

An observer on the orbital axis of a merging binary, at $\theta = \phi = 0$, will see a fully circularly polarized waveform where $\ell = |m| = 2$ is the only nonzero mode. An observer, however, in the orbital plane of the binary or the equatorial plane of the final black hole will see linearly polarized radiation with the contribution from $\ell = |m| = 2$ at its minimum. All other observers with intermediate orientations would see elliptically polarized waves that are combinations of all the modes. In practice, numerical relativity can only resolve a finite set of modes. Since the orientation of any given binary will be unknown *a. priori*, we analyze the templates' dependence on the detector's inclination and azimuthal angles in the source frame, as well as the variation of the signal-to-noise in each mode as a function of the source parameters. The location of the detector in the center of mass frame fixes the mode content and the orientation of the detector fixes the initial phase of the waveform.

The masses are set such that the overlaps will not change significantly if we were to add the inspiral portion of the signal. The change is minimal because for our A and B series of waveforms the orbital frequency increases almost monotonically. Owing to this, the gravitational wave frequency also increases monotonically with time implying that extending the signal back in time will not change the spectrum in the merger band. When precession is significant this will no longer be true and the inspiral will likely contribute to the signal at higher frequencies.

In this chapter, we focus our attention on how different initial configurations, in this case spin and initial spin orientation, result in different mode contributions to the signal-to-noise ratio. To build intuition about what parameters might be important to the template space of black-hole mergers, we calculate the overlap between pairs of our waveforms. We perform a preliminary analysis on how faithful $\ell = m = 2$ waveforms of various parameters would be in matching with waveforms at various detector inclination angles. The total mass for each template is kept fixed and the inclination angle of the detector, θ, the spin, a, and ϑ, the initial orientation angle of the spins with the orbital axis are varied as appropriate.

We also study the variation of the harmonic content with mass for the A-series waveforms. Before we study the numerical runs, it is useful to look at the expressions for the mode-content from the post-Newtonian approximation as well. These expressions can be useful in determining the dependence of the signal amplitude on the initial parameters such as a and ϑ.

5.2 Comparison to the post-Newtonian multi-mode distribution

One task facing the numerical relativist is to be able to locate the point at which post-Newtonian expressions for the waveform agree with the numerical relativity waveforms. While the waveforms we analyze are not long enough to be able to do this, we can certainly see the trends as a function of the initial parameters such as the spin magnitude and the orientation. The leading-order spin contributions to the various multipolar components can be derived by projecting the expressions for the waveform onto spin weighted spherical harmonics, according to the procedure described in [20, 19].

Let S_i be the projection of the spin of body i on the axis orthogonal to the orbital plane. S_i is positive (negative) if the spins are aligned (anti-aligned) with the orbital angular momentum. The dimensionless spin parameter $a_i = S_i/M_i^2$ $(i = 1,\ 2)$ and the spin combinations $\chi_s = (a_1 + a_2)/2$, $\chi_a = (a_1 - a_2)/2$. Including only the dominant spin-orbit (1.5PN order) and spin-spin (2PN) terms, in addition to the non-spinning terms one finds three spin-dependent multipolar contributions:

$$
\begin{aligned}
Mr\,\psi^{\text{spin}}_{2,2} e^{i\tilde{\phi}} &= 8\sqrt{\frac{\pi}{5}}\eta(M\Omega)^{8/3} \\
&\times \left[-\chi_s M\Omega + \frac{1}{2}(\chi_s^2 - \chi_a^2)(M\Omega)^{4/3}\right], \qquad (5.1)
\end{aligned}
$$

$$Mr\,\psi^{\text{spin}}_{2,1} e^{i\tilde{\phi}} = -\sqrt{\frac{\pi}{5}}(M\Omega)^3 \left[\chi_a (M\Omega)^{1/3}\right]. \qquad (5.2)$$

$$Mr\,\psi^{\text{spin}}_{3,2} e^{i\tilde{\phi}} = \frac{8}{3}\sqrt{\frac{\pi}{7}}\eta(M\Omega)^{10/3} \left[\chi_s (M\Omega)^{1/3}\right]. \qquad (5.3)$$

These expressions are a special case of the formulae in [19] for our specific configuration of equal-mass binaries. The value of χ_s is zero for our configuration and the $\chi_a = acos\vartheta$ in our notation. For the A-series these expressions predict that the odd modes would be linearly proportional to the magnitude of spin. There is no apriori reason to expect these post-Newtonian prediction to be valid in the late inspiral regime, just a couple of cycles prior to the merger. We test how powerful these predictions are for the waveforms considered.

5.3 Non precessing anti-aligned spin case: A-series

The resolution for this section will be fixed to the finest for the spin cases and the corresponding resolution for the non-spinning case. We use the minimax match as defined in Eq. (3.16), to see how different the $\ell = |m| = 2$ waveforms, given by $h(\theta = 0, \phi = 0)$, are from the full waveforms, $h(\theta, \phi)$, for a given a. Our focus is on θ, the inclination of the detector in the source frame since it causes a larger variation in the match than ϕ, the azimuthal angle. To reduce the number of parameters considered, and we set $\phi = \pi/2$ for the rest of the paper when $\theta \neq 0$. If we were to relax this condition, the minimax matches would vary on the order of a percent.

5.3.1 Variation of mode content with spin

The mode content for the anti-aligned spin cases is a function of the initial observer angle θ. To observe and study the variation with θ, we first fix the total mass for both templates, h_1 and h_2, to $100M_\odot$. In Fig. 5.1 we present the minimax matches as a function of a for templates at $\theta = \{0, \pi/4, \pi/3, \pi/2\}$. By holding the target template to

$\theta = 0$ for each spin case, we can determine at what angle and spin the matches drop below the threshold. In the case of $\theta = 0$, the templates have the same parameters and $M_{\text{minimax}} = 1$ as it must. For $a = 0$, all the templates match the $\theta = 0$ target within $M_{\text{minimax}} = 0.98$. The plot also indicates that $\theta = 0$ is close to the full waveform for $\theta \leq \pi/3$ for all of the spin cases. For $\theta > \pi/3$, however, the match drops below 0.98 for $a > 0.2$. As the inclination with the axis increases, the higher modes become important with increasing spin.

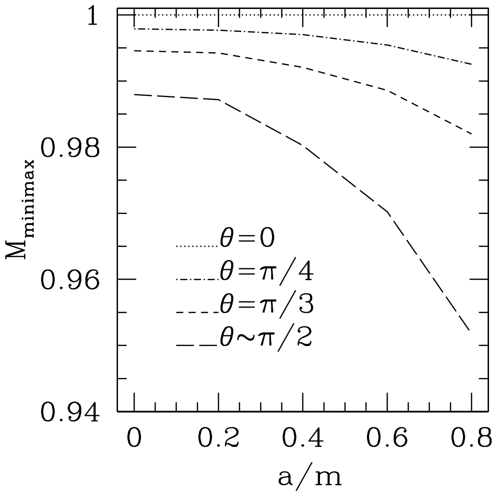

Fig. 5.1. The minimax match, $M_{\text{minimax}}[h_1(\theta = 0)], h_2(\theta_i)]$, vs a is plotted for the values $\theta_i = \{0, \pi/4, \pi/3, \pi/2\}$ for the case $m = 100M_{\odot}$.

In order to have a qualitative understanding of why the match behaves as in Fig. 5.1, we study the ρ per mode for the A-series. This is only a qualitative estimate because the relative fraction of modes present in the signal will depend on the relative spin-weighted spherical harmonics values at the particular angle. In practice the error induced by ignoring the mixed terms is less than 20%, as the relative overlaps of the significant modes from both the A and B-series of data are of this order. Since the ρ of the $\ell = 2$, $m = 2$ mode is much larger than the ρ of the other modes, we plot the ratio, $\rho(\ell, m)/\rho(2, 2)$ in figure 5.2. The upper left plot corresponds to a system of mass $50M_{\odot}$, the upper right to $100M_{\odot}$, lower left to $200M_{\odot}$ and lower right to $300M_{\odot}$.

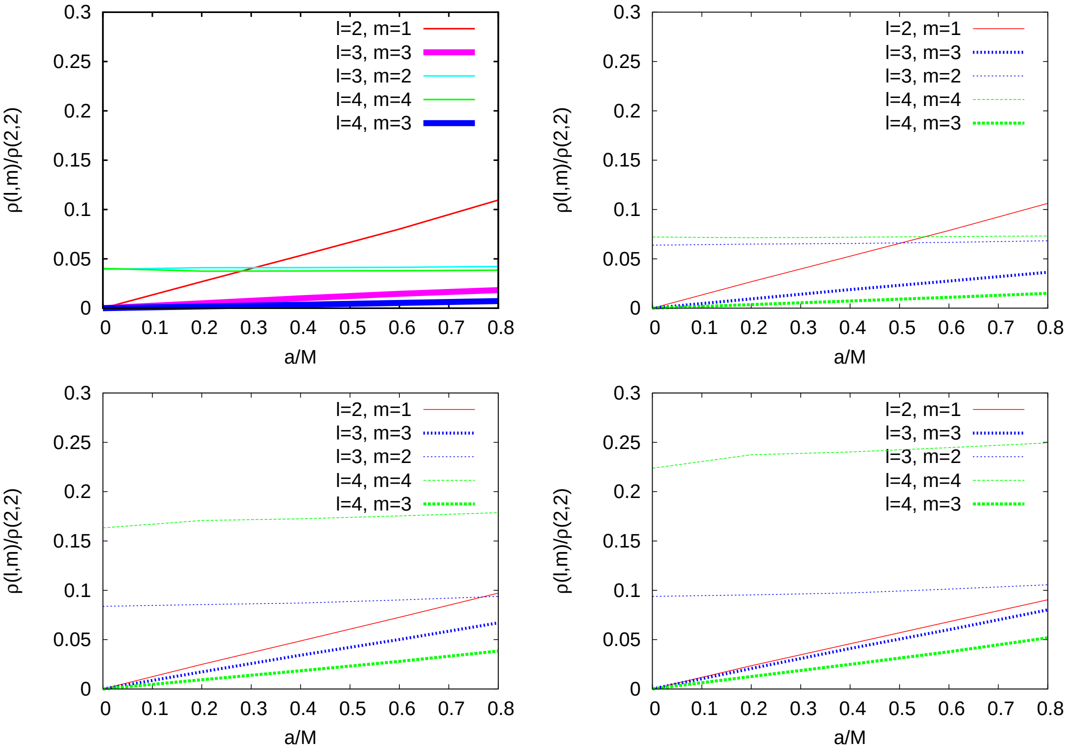

Fig. 5.2. A series of plots are shown with the ratio of ρ per mode to the ρ of the $\ell = m = 2$ mode versus the initial spin of the black holes. This is done for series-A. Each plot refers to the calculation for a different total mass of the binary. Starting from the upper left and moving right and then down, we have $50M_{\odot}$, $100M_{\odot}$, $200M_{\odot}$, and $300M_{\odot}$ on the lower right.

Across all the masses sampled, the ratio of the ρ for each mode grows with increasing spin. This is especially true for the $m = 1$ and $m = 3$ modes which are suppressed at low a. The $m = 2$ and $m = 4$ increase slightly with a. While the $\ell = 2$, $m = 1$ mode is the next mode dominant mode after the $\ell = m = 2$ mode for the high-spin regime at low masses, the $\ell = 4$, $m = 4$ is secondary for the entire a range at higher masses. For low spins, the waveform is entirely dominated by the $m = 2$ modes.

All of our results have errors attributed to the numerical computation used in computing the waveforms. In paper I, we analyzed the effects of resolution on the matched filtering technique and found that for the resolutions used to compute the waveforms studied here, the largest error would be ± 0.02 in the match, although that is only for the $a = 0.8$ case, and is typically smaller.

5.3.2 Variation of mode content with mass

To study inclination variation as a function of mass, we add the scale with total mass coming from the LIGO noise curve. We limit the presentation to two spins, $a = 0.2$ and $a = 0.8$ for clarity. The best, minimax and typical matches are plotted as a function of m in Fig. 5.3 and Fig. 5.4. The matches are between $h_1(\theta = 0)$ and $h_2(\theta_i)$ for three inclination angles each $\theta_i = \pi/4, \pi/3, \sim \pi/2$. We plot all three matches to demonstrate the range that the matches can take depending on the choice of phase optimization. The typical match is given by the lines and the minimax and best matches are specified as the lower and upper error bars respectively. One can see that the minimax match between the two templates sets a lower bound on the phase optimized matches. The minimax match dips below 0.98 for $\theta > \pi/3$ and $m > 100_\odot$ for both spin cases; and dips below 0.98 for the entire mass range for $\theta \sim \pi/2$ when $a = 0.8$. This result implies that using just the dominant mode and a 0.98 threshold would cause loss of the signal for angles greater than $\pi/3$. In fact, this result is potentially unexpected in how well the $\theta = 0$ template matches at angles less than $\pi/3$; however, as we evolve more cycles of the inspiral, we can expect this match to deteriorate. Additionally, the initial, non-precessing configuration of the black holes is likely resulting in less harmonic content in the waveforms which is in turn reflected in the match.

An even more stringent test is the best match. If the best match of a given angle waveform is smaller than some threshold then we would know that the higher modes are significant and need to be used in creating the template bank. We note that for both spin cases the best match is below 0.98 for $\theta \sim \pi/2$ at masses greater than $170M_{\odot}$ indicating the need to include higher modes to make a detection at large inclination and high masses.

One can see from the plots that the lower bound of the match between the circularly polarized and the highly elliptically polarized waveform is lower in the high mass cases. The decrease in the match at larger total masses may be indicating that the ring-down is more sensitive to the presence of higher modes than the merger itself, since the deviation from 0.98 is larger than expected from numerical error alone. These figures also suggest that the $\ell = |m| = 2$ mode is closer to the full waveform at lower masses and lower spins. The fraction of events lost by not including the higher modes needs to be calculated to predict the full impact.

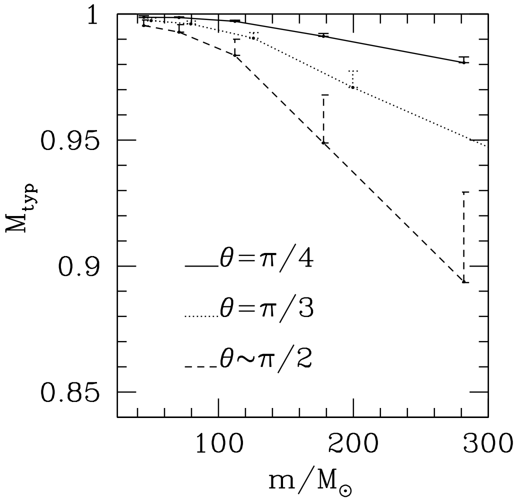

Fig. 5.3. The range of phase optimized matches between the $\theta = 0$ waveform and the full waveform for a low spin case, $a = 0.2$. The curves denote typical match $M_{\rm typ}[h_1(\theta = 0), h_{2+}(\theta_i)]$ for $\theta_i = \{\pi/4, \pi/3, \sim \pi/2\}$. The lower end of the error bar is given by the minimax match and the higher end is given by the best match. The phase optimization here is done over the phase of the h_1 template.

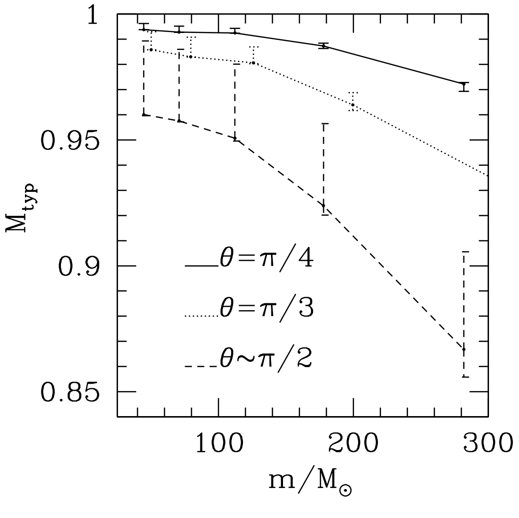

Fig. 5.4. The range of phase optimized matches between the $\theta = 0$ waveform and the full waveform for a high spin case, $a = 0.8$. The curves denote typical match $M_{\mathrm{typ}}[h_1(\theta = 0), h_{2+}(\theta_i)]$ for $\theta_i = \{\pi/4, \pi/3, \sim \pi/2\}$. The lower end of the error bar is given by the minimax match and the higher end is given by the best match. The phase optimization here is done over the phase of the h_1 template.

5.3.3 Variation with the extraction radius

The waveforms that we are using have been extracted from the numerical solution of the Einstein equation at a finite radius. In order to assess how the extraction radius, r_{ext}, affects the waveforms at a large extraction radius, we tabulate the M_{minimax} of the $a = 0.8$ waveforms in Tab. 5.1. Since the match carries more information than the signal-to-noise ratio in individual modes, we just present the match. The matches are computed for a template fixed at $\theta = 0$ and the target template at four values of θ to measure how much of the variation with θ depends on r_{ext}. The variation with the extraction radius is of the order of $\sim 1.3\%$ in the worst case. There is an interplay between better dynamical quality and increased numerical error as r_{ext} is increased, which is more noticeable in modes higher than $\ell = 2$. For the rest of the paper we use the waveforms at $r_{\text{ext}} = 30m$.

Table 5.1. Minimax matches for $m = 100M_{\odot}$ and $a = 0.8$ between two waveforms at the same extraction radius but different inclination angle given by $M_{\text{minimax}}[h_1(\theta = 0), h_2(\theta_2)]$.

r_{ext}	$\theta_2 = 0$	$\theta_2 = \pi/4$	$\theta_2 = \pi/3$	$\theta_2 \sim \pi/2$
30	0.9779	0.9602	0.9538	0.9518
40	0.9773	0.9530	0.9465	0.9519
50	0.9756	0.9473	0.9423	0.9546
60	0.9734	0.9445	0.9409	0.9564

We can see from this table that the higher modes deteriorate faster at closer radii.

5.4 The mode-content of B-series waveforms

The minimax match versus the initial angle for the B-series is presented in fig. 5.5. Each line represents a choice of total mass, with $50M_{\odot}$ the top most line and $300M_{\odot}$ the bottommost. The match was computed by setting one waveform to $\theta = 0$ and the other to $\theta = \pi/2.4$.

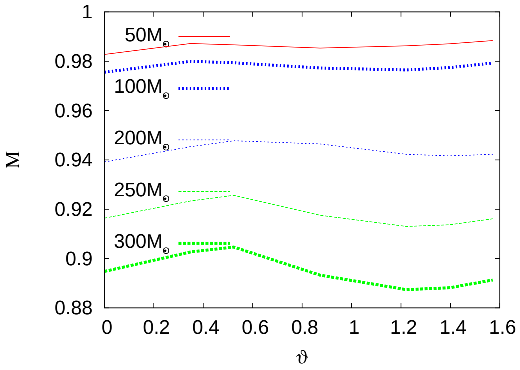

Fig. 5.5. The minimax match versus initial angle for the B-series. Each curve represents a particular choice of total mass, $50M_{\odot}$ at the top with each successively lower line a higher mass. To compute the match, we used one waveform with $\theta = 0$ and the other at $\theta = \pi/2.4$ radians for a given a and ϑ.

We find that the variation of the match across initial angle for the given spin of $a = 0.6$ does not change more than about 2%. The variation amongst different total masses is more dramatic, dropping down below a match of 0.9 for most in the angles at a mass of $300M_{\odot}$. At that large mass range, the ringdown is contributing significantly to the signal, and differences in the modes, like the $\ell = m = 4$ mode, begin to make important contributions. These BBH configurations settle down to a final black hole with a spin of $a = 0.62$.

In fig. 5.6, we once again investigate a qualitative interpretation of the match through the ρ as plotted versus the initial angle, ϑ for each mode. The upper left plot corresponds to a system of mass $50M_\odot$, the upper right to $100M_\odot$, lower left to $200M_\odot$ and lower right to $300M_\odot$.

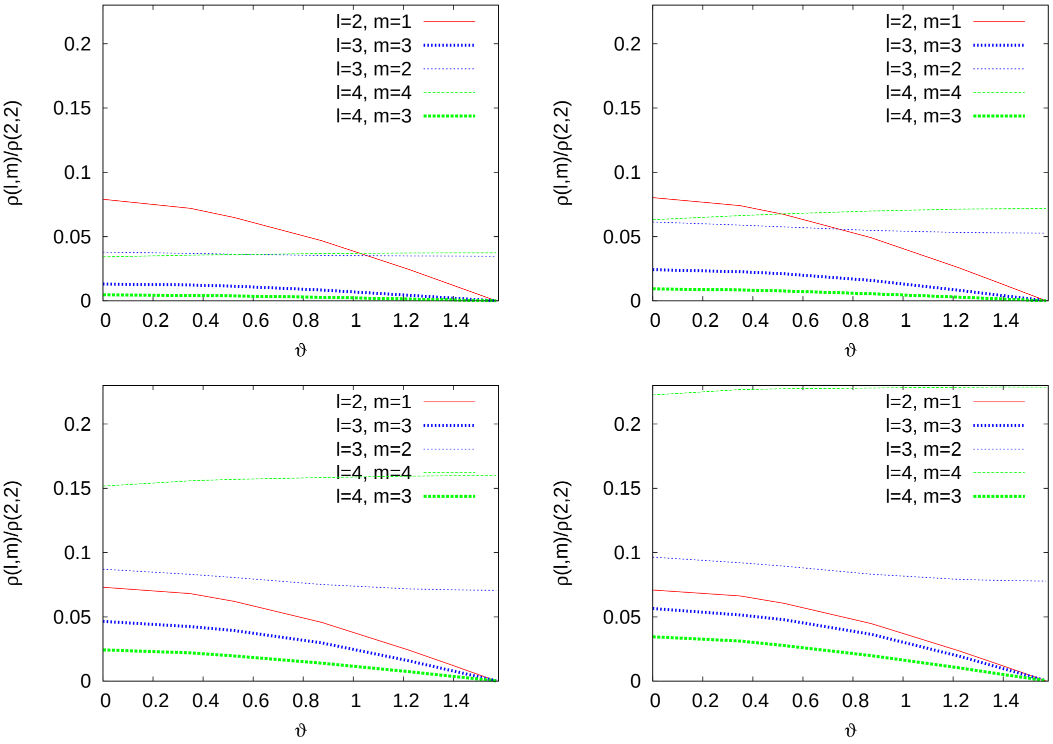

Fig. 5.6. A series of plots are shown with the ratio of ρ per mode to the ρ of the $\ell = m = 2$ mode versus the initial angle. This is done for series-B. Each plot is the calculation computed for a different total mass of the binary. Starting from the upper left and moving right and then down, we have $50M_\odot$, $100M_\odot$, $200M_\odot$, and $300M_\odot$ on the lower right.

Across the mass scales sampled, as the initial angle increases, the odd-m modes decrease. In the non-precessing case, the strength of the odd-modes is expected to vary with the z-component of the spin which is proportional to the cosine of the entrance angle. Since in this series of runs, the spins precess about the z-axis and ϑ remains constant, the relative strength of the modes show similar trends as the non-precessing case. At higher masses, where the ringdown dominates the signal, the $\ell = 4$, $m = 4$ mode is contributing a large portion of the ρ of the total signal, over 20% for a BBH of $300M_{\odot}$ total mass. It is interesting to note that in the "superkick" the spread of the modes is reduced in ρ compared with the parallel configuration at $\vartheta = 0$. The decrease of the odd m modes is expected. For example, the $\ell = 2$, $m = 1$ will be suppressed when the spins lie in the orbital plane for equal-mass black holes as discussed in [19].

5.5 Dominant mode versus full waveform for spinning binaries

We did a multipolar analysis of the modes in each waveform and calculated the signal-to-noise ratio of each mode versus the ρ in the $\ell = m = 2$ alone. For the A-series, the ρ per mode increased as the magnitude of the spins increased at every total mass. The odd-m modes increased from almost no contribution at low spins to a 10% contribution at larger spins. At a given spin, the $\ell = 2, m = 1$ mode dominated the ρ at low mass, but the $\ell = m = 4$ mode's ratio to $\ell = m = 2$ grew with increasing mass.

For the B-series, we found that the diversity of contributing modes decreases with increasing angle, except for the $\ell = m = 4$ and $\ell = 3$, $m = 2$ modes which remain relatively constant across ϑ for a given mass. As in the variation with a, at low total binary mass, the secondary signal is the $\ell = 2$, $m = 1$ mode, but at higher masses the

$\ell = m = 4$ and the $\ell = 2$, $m = 2$ modes are stronger. As anticipated, the $\ell = 2$, $m = 1$ mode decreases to zero as the initial angle moves to lie parallel to the orbital plane.

In this chapter we also include the variation of the match with the observer's inclination angle with respect to the source angular momentum axis. It is often convenient and instructive to extract the gravitational waveform, Ψ_4, decomposed into spin-weighted spherical harmonics as a function of ℓ and m. Including modes higher than the dominant mode, $\ell = |m| = 2$, is equivalent to allowing the inclination angle of the binary system to vary. Only at $\theta = 0$ would the $\ell = |m| = 2$ mode be the only harmonic in the waveform. The target waveform will have an unknown orientation; and, therefore we vary the inclination to study what effect this may have on detection. As we include all the modes in the analysis the match decreases, to as low as ≈ 0.85, must notably for larger masses and higher spins. Some decrease in match is expected since the higher modes require more resolution; however, the decrease was greater than that accounted for by the resolution alone.

We investigated the match between a waveform from the A-series containing only the $\ell = m = 2$ mode and a mode summed waveform. There we found strong dependence on the match with spin, with the $\ell = m = 2$ waveform failing to match to spinning waveforms especially for spins equal to and greater than $a = 0.6$. We did a similar study here for the B-series, comparing two waveforms of $a = 0.6$ at various ϑ. We found, despite the variation of the ρ versus ϑ, the match to not depend on the initial angle. The inclusion of modes was much more important to templates of higher mass, where the merger and ringdown dominate the signal, than at lower masses. This importance will be more evident in matches using unequal-mass and spinning waveforms with larger spin.

Chapter 6

Merger of Eccentric Binary Black Holes

6.1 Motivation: waveforms from eccentric binaries

It is well known that gravitational radiation leads to circularization of a binary system [45]. Although stellar mass BBHs will likely have completely circularized by the time they are observable by ground-based interferometers, scenarios have been suggested for which BBHs in eccentric orbits are not only astrophysically interesting but also could be detected by space- or ground-based interferometers [38, 59]. For instance, galactic mergers leave behind supermassive BBHs that likely interact with a gaseous environment. Such systems source for LISA. A gaseous-gravitational driven inspiral could yield a BBH arriving at the last few orbits and merger with a non-vanishing eccentricity. An observation of the gravitational waves from an eccentric BBH merger will allow us to determine the amount of angular momentum lost to gas and, in particular, the gravitational torques between the binary and the possible presence of a circumbinary disc that affect the eccentricity of the binary [12].

We study the circularization of an initially eccentric binary through gravitational wave emission in the dynamic, nonlinear regime. In Ref. [17], it was found that, for equal-mass, non-spinning black holes (BHs) initially in quasi-circular orbits, the merger produced a BH with spin parameter $a_{\mathrm{f}}/M_{\mathrm{f}} \sim 0.69$, which, within the accuracy of the results, was independent of the initial separation. In addition the authors found that, at

$t \sim 50\, M_{\rm f}$ before the amplitude of the gravitational wave reaches its peak, the BBHs enter a *universal* plunge during which the binary has lost "memory" of its initial conditions.

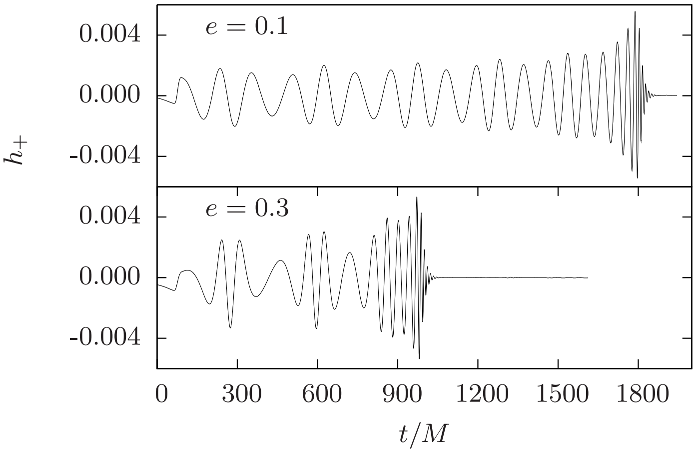

Fig. 6.1. Waveform polarizations h_+ for the cases $e = 0.1$ and $e = 0.3$

Similar results were also obtained by the AEI-JENA collaboration. In this chapter, our main goals are to investigate whether sufficient eccentricity is lost during the late stages of inspiral to circularize the orbit and exhibit the same *universality* as in the circular case and to extract the spin parameter and mass of the final BH, and compare the values with those from circular inspirals. We also investigate the distribution of the signal-to-noise ratio among the various multipole modes, and show that for optimally oriented binaries at identical distance from the detector, eccentric binaries can have a higher signal-to-noise than the circular ones.

The numerical simulations and results here were obtained with the same infrastructure used in our previous BBH studies (see Ref. [53] for full details). We have evolved the circular model at three different resolutions (finest grid spacings of $M/38.7$, $M/51.6$ and $M/64.5$). We obtain approximately fourth order convergence in the total energy and angular momentum radiated, consistent with the designed 4th order accuracy. The construction of initial data etc. are addressed in the next section.

6.2 Initial data for the eccentric runs

We construct initial data using the puncture approach [7], which requires specifying the coordinate locations and momenta for the two BHs. For "circular" orbits, we follow [8]. For eccentric models, we use the conservative 3PN expressions in Ref. [9]. These expressions require the specification of the eccentricity e and the mean motion $n = 2\pi/P_r$, where P_r is the radial (pericenter to pericenter) orbital period. There are three PN eccentricities, which are the same to 1 PN order, and we choose e_t, which appears in the PN Kepler equation, following Ref. [9]. It is important to keep in mind that the eccentricities we quote (and we use them also to label the models) are to be taken only as a guide to the eccentricity in the initial data, as the PN expressions used do not include radiation reaction, and the PN parameters are in a different coordinate system to the puncture initial data.

We construct a family of initial data by fixing $n = 0.01625/M$ ($P_r \sim 387M$) and varying e in the range $0.05-0.8$ to 2PN order, this means that the systems have the same binding energy and that, at high eccentricities, there are portions of the orbit for which the PN condition $v/c \ll 1$ is no longer valid. The binary separation D is determined from Eq. (23) in Ref. [9], and the tangential linear momentum, P/M, of each BH at apocenter is obtained from $J = PD$, where J is the total angular momentum computed as a PN expansion in n and e (Eq. (21) in Ref. [9]). The bare BH masses $m_{1,2}$ are chosen to make the irreducible BH masses $M_{1,2} = 0.5$ (i.e. $M = M_1 + M_2 = 1$). Table 6.1 provides the initial data parameters.

e	D/M	$P_{1,2}/M$	e	D/M	$P_{1,2}/M$
0.00	12.000	0.0850	0.40	18.459	0.0498
0.05	12.832	0.0792	0.50	20.023	0.0429
0.10	13.645	0.0741	0.60	21.539	0.0361
0.15	14.456	0.0695	0.70	22.955	0.0292
0.20	15.264	0.0651	0.80	24.072	0.0214
0.30	16.870	0.0571	–	–	–

Table 6.1. *Initial data parameters:* The runs are labeled by their initial eccentricity e. The BHs have linear momenta $\pm P_{1,2}/M$ and are separated by a coordinate distance D/M.

6.3 Final spin from eccentric mergers

We now discuss M_f and a_f, computed using two independent methods. In one method, they are obtained from the radiated energy and angular momentum using $M_f = M_{adm} - E_{rad}$ and $a_f/M_f = (J_{adm} - J_{rad})/M_f^2$. The subscript adm stands for the respective quantities calculated via the Arnowitt-Deser-Misner method calculating the respective quantities at null infinity as per standard prescriptions [**?**]. In the second method, $M_{\rm f}$ and $a_{\rm f}$ are computed from the quasi-normal mode (QNM) frequencies [22] emitted by the final BH, extracted using least squares fitting. As a cross-check, for some of the models we also determine $a_{\rm f}/M_{\rm f}$ using an approximate technique derived from the isolated horizon formalism [14]. Table 6.3 gives the energy $E_{\rm rad}$ and angular momentum $J_{\rm rad}$ radiated as well as the final mass $M_{\rm f}$ and spin $a_{\rm f}$. Fig. 6.2 gives the final mass $M_{\rm f}$ and spin $a_{\rm f}$ as a function of e. Notice the agreement in $a_{\rm f}$ and $M_{\rm f}$ that the three methods give within the estimated error bars. The final mass and spin also agree well in the circular case with the values obtained in Ref. [20].

e	$\frac{E_{\rm rad}}{M_{\rm adm}}$	$\frac{J_{\rm rad}}{M^2_{\rm adm}}$	$\left.\frac{a_{\rm f}}{M_{\rm f}}\right\|_{\rm rad}$	$\left.\frac{a_{\rm f}}{M_{\rm f}}\right\|_{\rm qnm}$	$\left.\frac{a_{\rm f}}{M_{\rm f}}\right\|_{\rm ih}$	$\left.\frac{M_{\rm f}}{M_{\rm adm}}\right\|_{\rm rad}$	$\left.\frac{M_{\rm f}}{M_{\rm adm}}\right\|_{\rm qnm}$
0.00	0.039	0.391	0.714	0.689	–	0.961	0.964
0.05	0.039	0.388	0.713	0.688	–	0.961	0.963
0.10	0.040	0.388	0.707	0.689	–	0.960	0.963
0.15	0.039	0.385	0.696	0.690	–	0.961	0.964
0.20	0.040	0.389	0.676	0.690	–	0.960	0.963
0.30	0.039	0.372	0.686	0.686	0.681	0.961	0.964
0.40	0.040	0.279	0.716	0.698	0.693	0.960	0.962
0.50	0.038	0.190	0.742	0.717	0.712	0.962	0.964
0.60	0.022	0.108	0.713	0.707	0.702	0.978	0.980
0.70	0.011	0.063	0.623	0.641	0.634	0.989	0.994
0.80	0.004	0.033	0.484	0.515	0.502	0.996	1.002

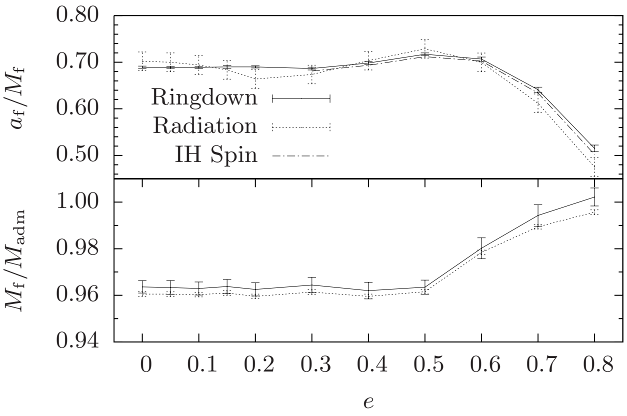

Fig. 6.2. Plots of $M_\mathrm{f}/M_\mathrm{adm}$ and $a_\mathrm{f}/M_\mathrm{f}$ as functions of the initial eccentricity e. Note that the error bars shown here on the radiation quantities for eccentric runs are copied from the $e = 0$ case and thus should be treated as indicative only.

Given an initial eccentricity, it is always possible to choose a large enough semi-major axis or orbital period for which the binary circularizes before it arrives at the merger. Our family of initial configurations was designed to investigate, for a fixed initial orbital period, how much initial eccentricity a binary is able to have and still enter the merger with essentially vanishing eccentricity. Since we do not have a good measure of eccentricity applicable prior to the merger, we focus on the end state, namely M_f and a_f of the final BH. We see from fig. 6.2 that $a_\mathrm{f}/M_\mathrm{f} \approx 0.69$ for $e \lesssim 0.4$ and $M_\mathrm{f}/M_\mathrm{adm} \approx 0.96$ for $e \lesssim 0.5$, both values of M_f and a_f in agreement with the circular result. We note that the remaining orbits, the ones which do not circularize, are all configurations which seem to plunge immediately rather than entering an orbital phase. We conclude that for the systems we studied with approximately constant initial orbital period, within our error bars, orbits with $e \lesssim 0.4$ essentially circularize before they merge, and orbits with $e \gtrsim 0.5$ plunge.

We also observe for $e \gtrsim 0.4$ that rather than a_{f} decreasing monotonically, a maximum spin parameter $a_{\mathrm{f}}/M_{\mathrm{f}} \approx 0.72$ is obtained around $e = 0.5$. Given the size of our uncertainties and that the maximum is found in the three independent methods used to calculate the spin, we are confident that this maximum is real for our family of initial data. At about $e = 0.6$, a_{f} starts decreasing monotonically. We are currently considering larger, but still computationally feasible, initial separations to investigate if there is *any* bound orbital (rather than plunge) configuration that does not circularize.

As $e \to 1$, corresponding to vanishing linear momenta (i.e. a head-on collision from rest), we find that $a_{\mathrm{f}}/M_{\mathrm{f}} \to 0$, in line with the symmetry of the head-on collision, and $M_f \sim M_{\mathrm{adm}}$, as expected, since NR simulations of a head-on collision have shown that $M_{\mathrm{f}} \sim (1 - 0.001)M_{\mathrm{adm}}$ [2]. Note that the ringdown result for $e = 0.8$ gives $M_{\mathrm{f}} > M_{\mathrm{adm}}$ which is clearly unphysical, but the error bars account for this.

6.4 Gravitational waves from eccentric binaries

In figs. 6.1 and 6.3 we display the gravitational wave strains and coordinate inspiral tracks for $e = 0.1$ and $e = 0.3$. The difference in initial eccentricity has a large effect during the inspiral. Qualitatively, the case with larger eccentricity exhibits a more rapid inspiral[45]. However, at some point both systems enter a “circular” plunge, hinting that circularization may have occurred. We find that the simulations with $e \geq 0.5$ show plunge-type rather than orbital-type behavior in the coordinate motion from the very start. Note that the tracks shown in Fig. 6.3 represent the *coordinate* positions of the individual BHs, and once a common horizon forms, they are less meaningful.

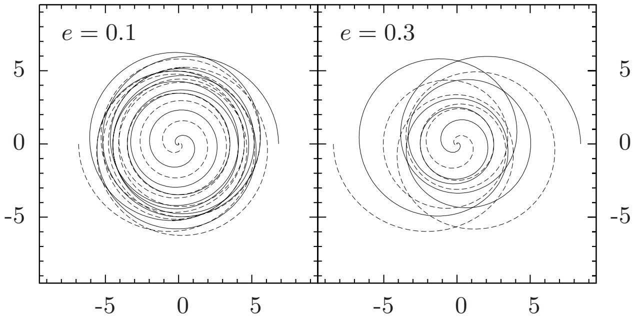

Fig. 6.3. Inspiral tracks for initial eccentricity $e = 0.1$ (left panel) and $e = 0.3$ (right panel).

We now consider the emitted radiation and focus on the dominant $\ell = 2$, $m = 2$ mode of the complex Newman-Penrose (NP) quantity $\Psi_4 = A(t) \exp(-i\varphi(t))$. To compare the orbits, we apply a time shift to A and φ as in Ref. [17], so the maximum of A (i.e. the peak of the amplitude of the gravitational wave) is at $t/M_{\mathrm{f}} = 0$ in each evolution. In Fig. 6.4, we plot the shifted amplitudes and frequencies $\omega = d\varphi/dt$ extracted at $r = 70\,M$. The cases displayed are those with eccentricities $e = 0 - 0.5$ in steps of 0.1 and $e = 0.8$.

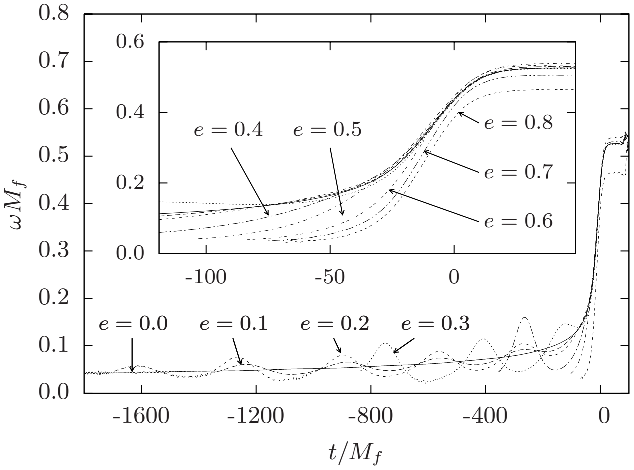

Fig. 6.4. Frequency of the $\ell = 2$, $m = 2$ mode of the NP radiation scalar $r\,\Psi_4$

In Fig. 6.4, the oscillations and growth in ω at early times (inspiral) can be in general terms understood from simple Newtonian considerations. That is, ignoring radiation reaction, the oscillations (i.e. amplitude and period) in ω are a direct consequence of the eccentricity and not present in the $e = 0$ case. The period of these oscillations is the period P_r of the extrema in the separation, and the amplitude of the oscillations increases with e. If one adds radiation reaction, the amplitude of the oscillations in ω decreases with time, corresponding to a reduction in eccentricity. As expected from the overall reduction in the binary separation, there is an overall growth of ω due to the energy and angular momentum loss. Also consistent with the predictions in [45], the higher eccentricity evolutions merge more quickly. We note that in the Newtonian case, we would observe that $P_r = P_\phi$, where P_ϕ is the time the binary takes to complete one revolution in the angular coordinate ϕ. Due to the effects of precession caused by GR, the two periods are very different (this can be seen from PN equations).

During the merger or plunge phase, ω increases dramatically and then levels off, signaling that the BBH has merged. After this point, ω remains constant, a direct consequence of the QNM ringing of the final BH.

As mentioned before, one of the objectives of this work is to investigate whether a given initial data configuration will circularize before it merges. By this we mean that the radiation from the late stages of the evolution is identical to that from an orbit which started with zero eccentricity. We see in Fig. 6.4 indications that the low e evolutions show the *universality* of a circular orbit at the very late stage of inspiral. The ω's from different eccentricities near the peak amplitude at merger seem to be indistinguishable for low enough eccentricity. In order to investigate this in more detail, in the inset of Fig. 6.4 we focus on the plunge stage. Here we plot eccentricities $e = 0 - 0.8$ in steps of 0.1. Up until $e = 0.4$ and after $t/M_{\mathrm{f}} \approx -50$, the frequencies ω from each run follow each other. Noticeable differences start showing for $e \geq 0.5$, which is the first configuration to plunge immediately without orbiting first.

6.5 Signal-to-noise ratio in the higher modes for eccentric binaries

There is a nonnegligible dependence of the signal-to-noise ratio on the eccentricity, especially near the transition point between inspiral and plunge. Before we analyse the signal-to-noise ratio and the fitting factors of the eccentric binaries with respect to a quasi-circular one, it is helpful to note the relative distribution of the signal-to-noise in the various spherical harmonic modes. This will also justify our choice of looking at just the optimally oriented binaries for further analysis. Notice how the ρ in $(4,4)$ mode has a significantly different variation with mass than the $(2,2)$ mode. The ρ near the $e \approx 0.5$ for higher masses, which is the transition point between the inspiral and plunge is consistently higher than the circular case by 20%. The $(2,0)$ mode contributes three times more in the nearly plunging case of $e = 0.8$, while for $e \leq 0.5$, its contribution is more or less independent of eccentricities. The $(3,2)$ and $(4,4)$ mode on the other hand show a greater variation with mass compared to the $(2,2)$ mode.

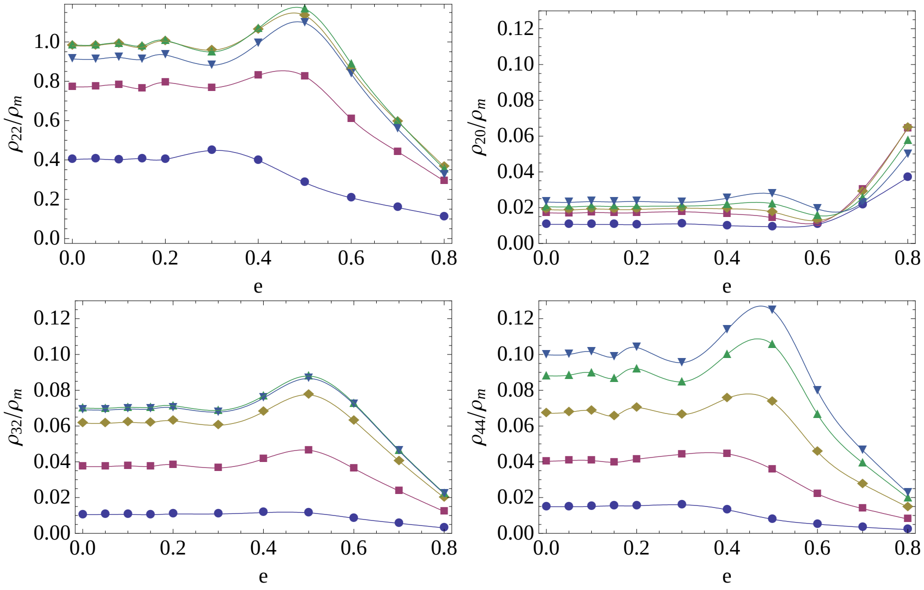

Fig. 6.5. The relative signal-to-noise in different modes of the eccentric waveforms. The (dots, squares, vertical triangles, diamonds and inverted triangles) represent the total masses $(40, 80, 120, 160, 200)M_{\odot}$ respectively. The top left[right] figure is for $(l, m) = (2,2)[(2,0)]$, bottom left[right] is for $(3,2)[(4,4)]$ modes respectively.

In fig. 6.5 we plot the signal-to-noise ratio as a function of eccentricity for a number of total mass values. The signal-to-noise is normalized such that the peak signal-to-noise ratio in the dominant mode of a non-eccentric binary is unity. This effectively amounts to fixing all the eccentric signals equidistant from the detector. The binaries are assumed to all have the same total mass. As we see below, for low eccentricities, other than the dominant ($l = |m| = 2$) mode the $l = |m| = 4$,$l = 3, |m| = 2$ and$l = 2, m = 0$ modes are the major contributors and carry less than $\approx 10\%$ of the signal for most cases. The interference between the modes can also constructively add up. To check this effect we also calculated the fitting factors between the full waveform at various inclination angles and the $l = m = 2$ mode and found that even for significant eccentricities ($e = 0.2$), the fitting factors were always> 0.95 even without maximizing over the mass. Thus the results for fitting factors calculated between just the dominant modes, should be valid to within $\approx 5\%$ for an arbitrarily oriented source for low eccentricities $e \leq 0.2$. For higher eccentricities ($e\tilde{0}.5$) the mode content is a few percent higher, and the error will be slightly higher, but one can even in this case the errors should not be higher than of the order of 10%. For ease of presentation we shall ignore the higher modes and assume optimal orientation in the signal as well as templates, which in practice implies using just the $\ell = m = 2$ mode.

The variation in ρ with eccentricity is depicted as a contour plot in fig. [**?**] where we have removed the previous normalization. The contours correspond to the physical scale and we see that there is significantly more signal from an eccentric binary of $e \approx 0.5$ than a quasicircular binary at identical distance. This relationship can be inverted to infer that an eccentric binary $e \approx 0.5$ can be seen to slightly greater distance ($20 - 25\%$

farther) than a circular binary. This will increase the detection volume in which an eccentric binary can be detected by a factor of $1.8 - 2.4$ compared to that for a circular one. This assumes matched filtering of an eccentric binary merger signal with an identical eccentric template. In practice, it would be important to know how different are these signals when matched to a quasicircular template, and if a template bank consisting of quasi-circular templates will be successful in capturing these mergers with residual eccentricity in the last few orbits. This forms the subject of our next section.

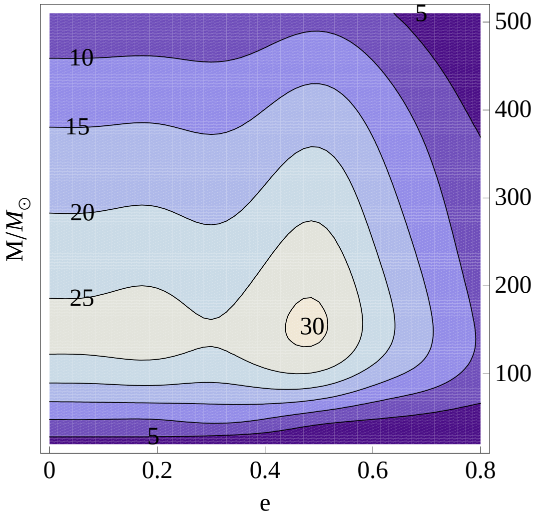

Fig. 6.6. For a threshold signal-to-noise of 10, the contours of the maximum distance reach(also called the signal horizon) in the (Mass, eccentricity) parameter space. The contours are labeled in units of 10 Mpc to facilitate display.

6.6 Conclusion

We have carried out a series of eccentric orbit simulations of BBH to investigate the merger dynamics in the non-linear regime and to determine the final state of the system. The family of simulations consisted of binaries with approximately constant initial orbital period and varying initial eccentricity. We found that for initial $e \leq 0.4$, the final BH parameters are $M_{\rm f}/M_{\rm adm} \approx 0.96$ and $a_{\rm f}/M_{\rm f} \approx 0.69$, the same as in the circular case. We also find that for $e \leq 0.4$ the binary begins to enter a *universal* plunge at $t \sim 50\, M_{\rm f}$ before the amplitude of the gravitational radiation reaches its peak, as observed in the circular case. In a sense, one effect is a consequence of the other. Namely, the emergence of a *universal* plunge implies that the final state of the system, i.e. the final BH, is "unique." Reaching the same final state is also a strong indication that the binary has circularized by the time it enters the plunge.

We also examined the distribution of the signal-to-noise in various modes and found that the signal to noise in the dominant mode among different eccentric binaries seemed to peak at $e = 0.5$, the eccentricity beyond which there seemed to be only a plunge phase. This results in being able to see an eccentric event with eccentricities in the regime $(0.4, 0.55)$ farther out than one can see a circularized binary. In the next chapter we shall present a preliminary investigation of how efficient the quasicircular merger templates to be used in LIGO are for detecting eccentric binaries.

Chapter 7

Detection of spinning and eccentric binaries

7.1 First steps toward detecting generic IMBH mergers

At the time of writing this, the search strategies used in the LIGO inspiral group for binary black hole coalescences employ the so-called restricted post-Newtonian waveforms for quasi-circular orbits. While there are detection template families that are designed to capture the spin precession in the inspiral case, the issue of searching for the merger/ringdown phase of these waveforms is still yet to be properly addressed. There is work in progress to test the use of full NR waveforms in both inspiral and burst detection schemes . This has the potential of extending the upper mass limit of searches for initial LIGO from $30M_{\odot}$ to $200M_{\odot}$ depending on the type of waveform being used.

In a general astrophysical scenario such as an IMBH binary in a stellar cluster, it is possible to conceive of a generic binary with both non-zero eccentricity as well as arbitrary spin orientation. Although there are claims that the spins of the binary will get aligned to the angular momentum owing to friction with gaseous environment, the so-called "wet merger" scenario, it is possible that there maybe some mergers with arbitrarily aligned spins. Our approach in examining the detectability of a generic merger of an intermediate mass binary is to first consider an equal mass spinning binary with anti-aligned spins and check the effectiveness of a non-spinning as well as moderately spinning template in searching for it. Next we examine a non-spinning but eccentric equal-mass binary merger signal, and examine how well a numerical quasicircular ($e \approx 0$) merger waveform can capture such a merger. This are preliminary attempts at learning how numerical relativity templates may become a tool for astrophysical discovery.

7.2 Observing the spin in merging binaries

7.2.1 Comparing waveforms of different non-precessing spins

Computing the full solution to the BBH problem is computationally expensive, an expense that increases as the spins increase and the mass-ratio decreases. To learn if we can alleviate some of this computational expense by fore-knowledge of the density of the required template space, we investigate how well a specific template matches a target template of arbitrary spin and inclination angle. The resolution is held fixed at ($\Delta = m/40$). We will study several cases, including spin configurations relative to each other at different inclination angles for a fixed mass of $100M_\odot$ and then we specialize to a few angles and study the typical, minimax and the best phase optimized matches.

The simplest approach to compare the spinning waveforms is to fix the observer inclination angle $\theta = 0$ for both the target and template waveform. We then choose the template to have some spin and calculate the match of that template with a target that varies with the spin a of the black hole. Specifically we focus on $M_{\text{minimax}}[h_1(a_i), h_2(a_j)]$ where a_i and a_j run over all the combinations of spin. The minimax matches between all combinations of the spins are ≥ 0.995 over the mass range considered. This reflects the fact that the binaries approach the same final black hole and that the initial spin gets radiated away in modes other than $\ell = |m| = 2$, where they are almost identical during the late stages of the binary merger (sometimes called universality [15]). The dominant modes of non-spinning and anti-aligned spinning waveforms are thus indistinguishable hinting that the non-spinning case may be sufficient for a detection but potentially making parameter estimation problematic. This degeneracy with spin, however, does not hold when we include more radiation modes.

We explore the matches between different spin templates at different inclination angles, considering first the templates with a fixed mass of $100M_{\odot}$. The variation of the minimax match between a template of $a = 0$ and target templates that vary with a is presented in Fig. 7.1 and with both the template and target varying with $a \neq 0$ in Fig. 7.2. In terms of the match, Fig. 7.1 corresponds to a minimax match, $M_{\text{minimax}}[h_1(a = 0), h_2(a_i)]$, and Fig. 7.2 between six combinations of the four spinning configurations, $M_{\text{minimax}}[h_1(a_i), h_2(a_j)]$ both versus θ. In both figures, at $\theta \leq \pi/3$ the template is within a M_{minimax} of 0.98 with the targets, making them indistinguishable. When the template is fixed at $a = 0$ in Fig. 7.1, the match is > 0.98 for all θ except with $a > 0.6$, which shows a stronger drop-off with angle for higher initial spins. Fig. 7.2 shows that the matches between adjacent templates among the $a = \{0.2, 0.4, 0.6, 0.8\}$ group are better than 0.99, while the matches that have a spin parameter difference $a_1 - a_2 \geq 0.4$ drop below 0.98 at higher angles. These templates are based on short waveforms of just two and a half cycles and the matches will likely get worse when more cycles are included. We conclude from these plots that the $\ell = |m| = 2$ mode continues to dominate the other modes at small angles, $\theta < \pi/4$, leading to similar matches between a spinning and non-spinning configuration. As the inclination angle grows, however, the presence of higher modes becomes more pronounced, breaking the degeneracy between the waveforms from different initial spin configurations.

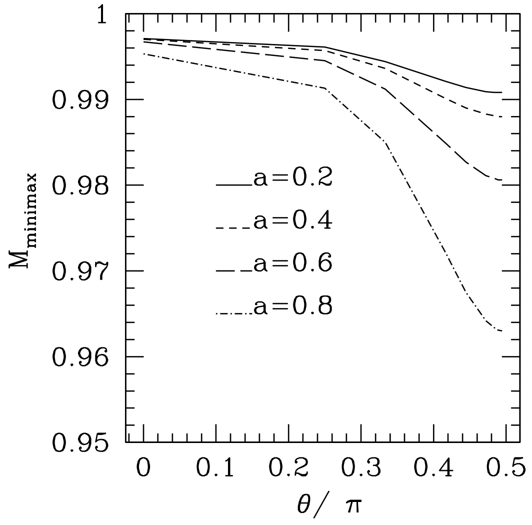

Fig. 7.1. The minimax match $M_{\text{minimax}}[h_1(a=0), h_2(a_i)]$ as a function of θ between the waveforms of different spins at the same resolution $m/40$, with the non-spinning waveform at resolution $m/38.4$. The mass of the final black hole for all the cases is $100 M_\odot$ and the spins run over $a_i = \{0.2, 0.4, 0.6, 0.8\}$. Note the monotonic decrease of the match with angle.

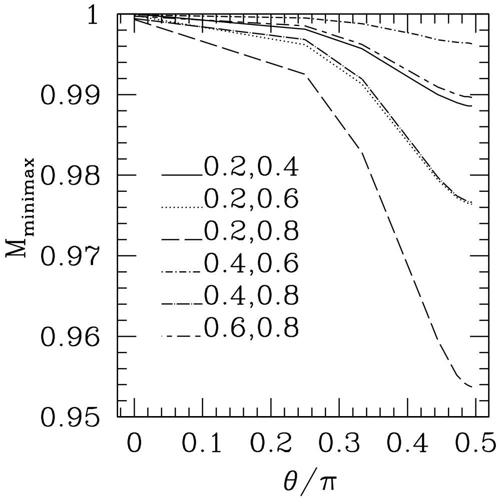

Fig. 7.2. The minimax match between the waveforms of different nonzero initial spins, $M_{\mathrm{minimax}}[h_1(a_i), h_2(a_j)]$ as a function of θ. The mass of the final black hole for all the cases is $100M_\odot$ and $\{a_i, a_j\}$ runs over $\{0.2, 0.4, 0.6, 0.8\}$. Note the monotonic decrease of the minimax match with the angle θ.

For completeness, we present the table of the range of values over which the phase optimized matches of the different spinning waveforms can vary in Tab. 7.1. These matches are evaluated at $\theta \sim \pi/2$ to report the widest range of matches calculated. The table indicates that the range of matches is higher at lower masses and tends to decrease with mass.

To place the minimax matches between the spins in context with the typical and the best matches, we present the typical match $M_{\mathrm{typ}}[h_{+1}(a = 0), h_2(a = a_j)]$ for

Table 7.1. The range of phase optimized matches reported as $\left(M_{\text{minimax}}, M_{\text{best}}\right)$ between two templates of various spin pairs $\left(a_1, a_2\right)$ where both templates have $\theta \sim \pi/2$.

(a_1, a_2)	$50M_\odot$	$120M_\odot$	$300M_\odot$
$(0.0, 0.2)$	$(0.8940, 0.9513)$	$(0.9228, 0.9618)$	$(0.9446, 0.9701)$
$(0.0, 0.4)$	$(0.8570, 0.9507)$	$(0.8882, 0.9604)$	$(0.9141, 0.9684)$
$(0.0, 0.6)$	$(0.8595, 0.9530)$	$(0.8898, 0.9618)$	$(0.8234, 0.9427)$
$(0.0, 0.8)$	$(0.7325, 0.9196)$	$(0.7896, 0.9326)$	$(0.8369, 0.9449)$
$(0.2, 0.4)$	$(0.9860, 0.9964)$	$(0.9884, 0.9967)$	$(0.9858, 0.9954)$
$(0.2, 0.6)$	$(0.9742, 0.9927)$	$(0.9751, 0.9927,)$	$(0.9665, 0.9912)$
$(0.2, 0.8)$	$(0.9526, 0.9832)$	$(0.9497, 0.9793,)$	$(0.9194, 0.9681)$
$(0.4, 0.6)$	$(0.9973, 0.9993)$	$(0.9959, 0.9988,)$	$(0.9945, 0.9971)$
$(0.4, 0.8)$	$(0.9808, 0.9956)$	$(0.9732, 0.9902,)$	$(0.9611, 0.9738)$
$(0.6, 0.8)$	$(0.9911, 0.9982)$	$(0.9880, 0.9950,)$	$(0.9824, 0.9867)$

$a_j = \{0.2, 0.8\}$ and $\theta = \{\pi/2, \pi/4\}$ in Fig. 7.3. The error bars are given by the minimax and the best match in order to demonstrate their variation with mass. As seen in Fig. 7.3, the difference between the minimax and best matches is slight at small values of θ and a, while for large angles it can vary over the order of $\sim 3\%$. The variation is much higher at lower masses because there are more cycles in the sensitive part of the LIGO noise curve making the match more sensitive to the relative phasing of the templates. The figure indicates that using a non-spinning waveform as the template in detection would cause the largest losses when the target has large spin and angle.

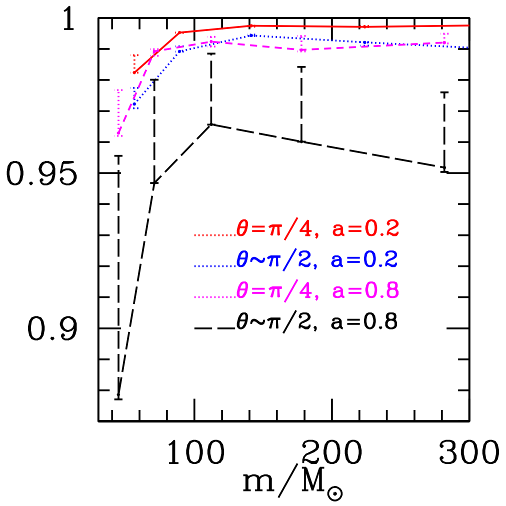

Fig. 7.3. We plot the range and the typical values of phase optimized match between the waveforms of different initial spins, $M_{\rm typ}[h_{+1}(a=0,\theta_j), h_2(a_i,\theta_j)]$ as a function of mass where $a_i = \{0.2, 0.8\}$ and $\theta_j = \{\pi/4, \pi/2\}$.

7.2.2 Comparison between non-spinning template and spinning signal

We have seen the variation of the match between templates of the same spin parameters and different angles and different spin parameters and the same angle. In setting up a template bank using these numerical waveforms, it may be useful to know if just a couple of templates at some specific inclination and spins can cover the whole set of waveforms considered here.

For this study we calculate the minimax matches between a template of a given value of spin and inclination angle and a target with a spin parameter varying over $a_i = \{0.0, 0.2, 0.4, 0.6, 0.8\}$ and a fixed, but different inclination angle. In Fig. 7.4 we plot the variation of the minimax match for a template with $a_1 = 0.0$ and $\theta_1 = \pi/4$ with target templates of varying spin and $\theta_2 \sim \pi/2$ as a function of total mass. We made the choice of the template to have $\theta_1 = \pi/4$ since we have concluded that a choice of $\theta = 0$ is going to fail to match well over a range of target inclination angles, especially at lower masses. We choose the target template to have $\theta_2 \sim \pi/2$ to calculate the worse case scenario for the inclination angle of the target. In Fig. 7.5 we substitute a template of $a_1 = 0.4$ and keep all the other parameters the same as in Fig. 7.4. This improves the matches at smaller total mass. One can see from the figures that the higher the match threshold, the smaller the mass range covered by the template. A coarse template bank would do better with $a = 0.4$ and $\theta = \pi/4$ than $a = 0$ at the same $\theta = \pi/4$ especially for the lower masses and hints that there may be an optimal way to lay out this template space. Another feature is that for higher masses, the matches for both the cases look similar, as the late-merger/ringdown has some universality-independence from the initial spin.

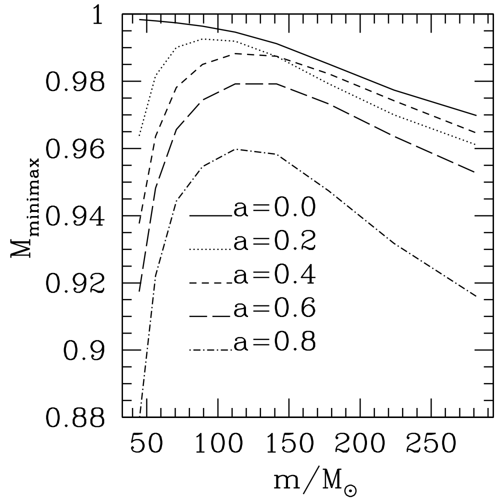

Fig. 7.4. We plot the minimax match between the target templates of different initial spins at a fixed θ with a template of $a = 0.0$, $M_{\text{minimax}}[h_1(a = 0, \theta = \pi/4), h_2(a_i, \theta = \pi/2)]$ as a function of mass. Notice the low matches at the smaller masses.

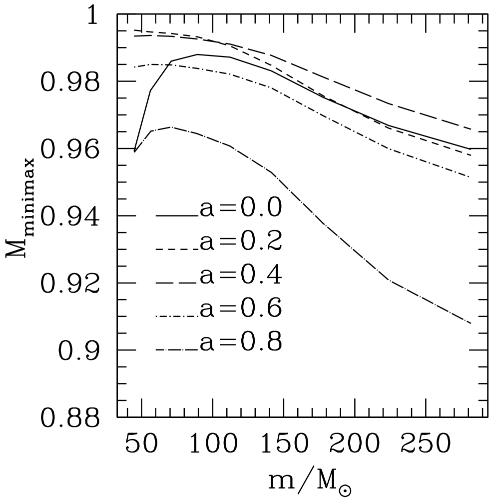

Fig. 7.5. We plot the minimax match between the target templates of different initial spins at a fixed θ with a template of $a = 0.4$, $M_{\rm minimax}[h_1(a = 0.4, \theta = \pi/4), h_2(a_i, \theta = \pi/2)]$ as a function of mass.

The use of these axial-spin waveforms as templates for detection has some limitations. The waveforms investigated here are from a non-precessing, anti-aligned configuration, the study in case of precessing binaries with arbitrary spin configurations will be the subject of a future work. It is likely that the higher radiation modes will play an even bigger role than they do for the relatively simple case investigated here. The major limitation however, is the small number of gravitational wave cycles present in the waveforms. The ISCO frequency is about $0.02/m$. The mass at which the ISCO frequency hits the seismic wall of LIGO noise curve of $40\,{\rm Hz}$ is about $100M_\odot$. If one allows the lower limit in the match integrals to vary or be fixed at $0.02/m = 70\,{\rm Hz}$ for example, then we can trust these matches up to $\approx 60M_{\odot}$ assuming that we will search for events that are merging in the LIGO band with little to no inspiral. Although the results will not change too much at high masses even if inspiral is included in the numerical templates, low mass results are expected to have lower matches. Finally, another limitation of these matches is that it assumes identical total mass for the template and the waveform being compared to it. This assumption needs to be relaxed to estimate the "effectualness" of templates for detection, which will be done in a future work.

7.3 Observing the eccentricity in binary black holes with non-eccentric templates

7.3.1 Motivation and Previous work

If there are mergers of binary black holes with residual eccentricity, the searches with post-newtonian or even *hybrid* (post-Newtonian + numerical relativity) templates assuming a quasicircular orbit will miss some of the events. The extent of such losses was first investigated by Martel and Poisson, [36]. They matched phenomenological circular quadrupolar waveform templates to match with target waveforms from some nonzero eccentricity orbits with binaries of different mass ratios. They found that for a given eccentricity the loss of snr decreased with increasing mass and for a given mass the loss of snr increased with increasing eccentricity. Recently, this problem was reanalysed by Tessmer and Gopakumar [51] using higher order post-Newtonian waveforms. They found that the conventional quasi-circular waveforms did not give appreciable matches with 2.5 PN eccentric waveforms, but taking the $e \rightarrow 0$ limit of the eccentric waveform evolution equations gave waveforms that had fitting factors > 0.96 for $e < 0.1$ for a $(10+10)M_\odot$ binary.

One possible source for ground-based detectors is the intermediate mass binary black holes, with mass range $30 \leq M/M_\odot \leq 300$ [30]. While the generation mechanisms for such mass ranges are uncertain, it is possible that the mergers that form such binaries leave some residual eccentricity in the binaries. For these mergers the leading contribution to the signal to noise ratio will come from the last few orbits pre-merger and the ringdown phase post-merger, and the waveforms for these can only be obtained by numerically solving the Einstein equations on a supercomputer. Given the recent revolution in the field of numerical relativity, several binary black hole orbits can now be evolved all the way up to the coalescence and the waveforms are available for several different initial parameter choices such as different spins, spin orientations, mass ratios, and also eccentricities. It is now possible to start at separations far enough that 3.5 PN waveforms can be matched to the numerical ones in the inspiral regime for the non-spinning BBHcase. This leads to the possibility of constructing merger waveforms phenomenologically by using a semi-analytic fit of these numerical waveforms.

Phenomenological templates to cover the complete waveform including the inspiral, merger and ringdown have been constructed by different collaborations (Ajith et al and buonanno et al). These templates will extend the reach of the detectors beyond the $30-40M_\odot$ limit which the inspiral waveform templates offer. A natural pipeline that will emerge soon from the NINJA (Numerical Relativity Injection Analysis group) to cover the massive and intermediate mass binary merger searches in LIGO will incorporate the numerical relativity merger/ringdown waveforms in some form or other.

The effect of the eccentricity in the last few orbits on waveforms has been studied and the seemingly weak dependence of the final black hole spin on the initial orbital eccentricity has been observed in $3d$ numerical evolutions of Einstein equations. The last few orbits will contribute significantly to the signal to noise ratio only for massive and intermediate mass black hole binaries, and not as much for the stellar mass ones. How efficient would a pipeline incorporating the quasi-circular numerical relativity merger waveforms be in detecting the merger of an eccentric IMBH binary that merges in the LIGO band? In the last few orbits naively one would expect the radiation reaction and hence the effect of orbital eccentricity to increase, leading to significant phase and amplitude differences between quasi-circular and eccentric waveforms. A search that uses just a circular templates should thus be less efficient in capturing eccentric waveforms. However, the weak dependence of the final spin on the initial eccentricity suggests that the circular templates for the last few cycles may be able to detect a significant range of eccentricity with just a mild loss of signal-to-noise. As we shall see below, both these statements are true, the former for low masses for which the first part of the late inspiral dominates and the latter for high masses wherein the plunge and ringdown dominates with respect to the LIGO noise.

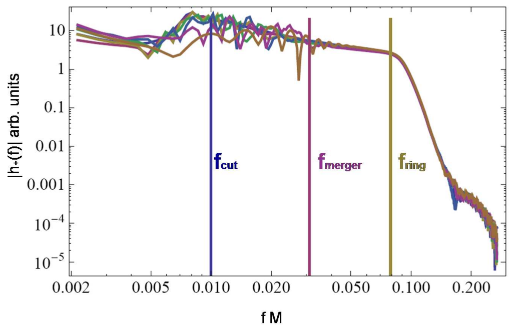

Fig. 7.6. The spectra for eccentricities $0, 0.05, 0.1, 0.15, 0.2, 0.3$ to illustrate three distinct regions of the spectrum-late inspiral, universal plunge/merger and ringdown. The x-axis here is in code units of frequency which scales inversely as mass.

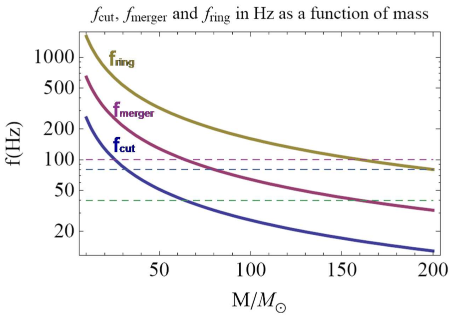

Fig. 7.7. The physical frequency corresponding to the three regions demarcated in the previous figure, to give an idea of the frequency scales involved.

7.3.2 Fitting factors of eccentric merger signals with non-eccentric templates

In what follows we shall restrict attention to equal mass binary black holes. Consider optimally oriented eccentric binaries with differing specification of initial eccentricities at the same distance from the detector and with the same detector orientation. The search templates are "complete" quasi-circular waveforms which could be parametrized models in principle, such as (Ajith, buonanno1, buonanno2) or hybrid waveforms constructed by joining Post-newtonian waveform to the numerical one.

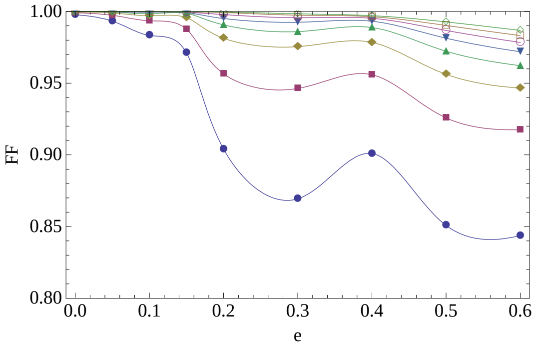

Fig. 7.8. The fitting factors as a function of eccentricity. The curves correspond to differen total binary mass $M_{signal}/M_{\odot}$ of the signal waveform: filled circles-60,squares-80, diamonds-100, upright triangles-120, inverted triangles-140, open circles-160, open square-180, open diamond-200.

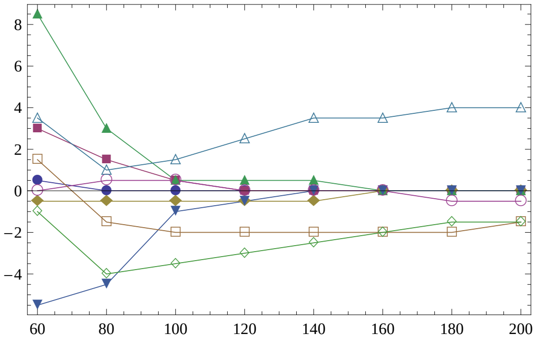

Fig. 7.9. The fractional error in mass parameter for different eccentricities as a function of mass, in percent. There is greater error at lower masses, even for low eccentricities. Each set of errors corresponds to different eccentricity of the signal waveform: filled circles-0.05,squares-0.1, diamonds-0.15, upright triangles-0.2, inverted triangles-0.3, open circles-0.4, open square-0.5, open diamond-0.6.

In practice, since the circular $e = 0$ run starts at lower angular frequency than the eccentric ones, we use our largest separation, circular numerical waveform as the template and calculate the fitting factors for the series of eccentric waveforms. If we had longer eccentric waveforms, and if we wished to probe the low mass region of the parameter space, then it would be imperative to extend the template. The signals consist of the different eccentric waveforms. We plot in fig. 7.8 the fitting factors optimized over the mass of the circular template as a function of eccentricity for various mass values of the signal. The fitting factors seem to monotonically increase with mass and show an almost monotonic decrease with eccentricity.

Overall it is interesting to note that for masses less than $30M_\odot$ the fitting factors of low eccentricities ($e < 0.1$) are high (more than 0.9). With higher masses, the range of eccentricities covered by the circular templates increases almost monotonically. The oscillation seen around $e = 0.4$ is owing to the fact that beyond this eccentricity the orbits just plunge without finishing an orbit for the initial data used. While the value of initial eccentricity is dependent on the separation specified, what this demonstrates is that even for pretty high eccentricities, quasicircular templates are remarkably efficient at covering the merger/ringdown for massive binaries $M > 60M_\odot$ say. Overall one could attribute the fact that the circular templates covers the eccentric parameter space so well to universality however this is unclear if we look at the way the cut off frequencies and the universality scales.

7.3.3 The impact on actual event loss rate

As we saw in the previous chapter, given a signal to noise threshold of 10, the signal from an eccentricity in the transition regime ($0.4 < e < 0.55$) can be seen a few tens of percent farther out than a circular case. Assume a uniform distribution of merger events over little more than the detection volume accessible for the circular case. Further assume that the events from all eccentricities are equally probable. Then, the detection rate of the eccentric binaries will be accordingly higher compared to the circular ones. We can see this behaviour in the figure 7.10 where the first figure is the fractional difference in the detection volume of an eccentric signal compared to a circular signal assuming a template identical to the respective signal. In an actual detection scenario however, the signal-to-noise will be diminished by the fitting factor with nonoptimal template used to detect these eccentric binaries. the volume will diminish by a factor FF^3.

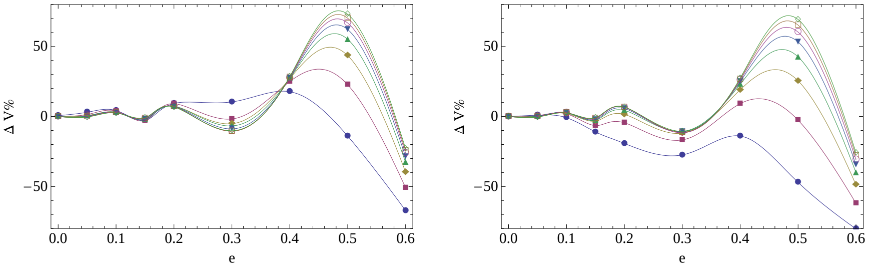

Fig. 7.10. The percent fractional difference in detection horizon volume relative to quasi-circular signals as a function of eccentricity. The reduction in detection volume because of using non-eccentric templates is most noticeable for total binary mass $M_{signal}/M_{\odot}$ of $60M_{\odot}$ indicated by filled circles and filled squares-80 .

In this case the fractional difference relative to the quasicircular case in the detection volume is given by the figure on the right panel of fig. 7.10. The left figure is for the case when the templates used are identical to the eccentric signals and the right figure to the case when the quasi-circular templates are used to detect the eccentric signals. If we assume all eccentricities are equally probable, this will be the same as the fractional difference in event rate.

As we can see for masses $> 100M_\odot$, there is no noticeable difference between the detection volumes. For lower masses like $60M_\odot$ the nonoptimal nature of the template can cause as much as 10% of the detection volume and perhaps the same event rate loss.

7.4 Effectiveness of non-eccentric, non-spinning templates

Our aim in this chapter was to determine the efficiency of a search which neglects the spin and eccentricity in the binary black hole waveform signals.

In light of the computational effort involved in searching over large, densely populated template banks, we calculate the match between waveforms of different initial spin to see if a reduced set of spinning waveforms would be good enough. The waveforms we use in this analysis evolve toward the same Kerr black hole ($a \approx 0.66$) even though the initial spins of the individual black holes vary from 0.0 to 0.8 because of the fixed initial ADM angular momentum. This results in very high matches $M_{\text{minimax}} > 0.99$, between all the spinning and non-spinning waveforms for the dominant mode. Without adding information from the higher radiation modes, all the spinning BBH waveforms appeared the same in terms of matched filtering.

Once h was constructed using the modes $\ell < 5$ which were resolvable over numerical noise in the BBHsimulations, this degeneracy broke. We constructed two "typical" cases, one in which the template had a fixed $\theta = \pi/2$ and $a = 0$ and the other $a = 0.4$. The templates were matched against a target template also at $\theta = \pi/2$ for each spinning waveforms. When $a = 0$, the matches were as low as 0.88 versus m, but were > 0.95 for $m > 100M_\odot$. By choosing an intermediate spin of $a = 0.4$, the matches were improved for the lower masses, $m < 100M_\odot$, increasing the lowest value from 0.88 to 0.96. We speculate that this indicates that there may be an optimal layout for the template space for a coarse search over spins. The matches were always at their highest at $100M_{\odot}$, although not necessarily greater than 0.98.

The issue of whether or not a quasicircular template will be effective in detecting an eccentric signal on the other hand, seemed to have been resolved in the favor of affirmative ref. [36]. For low eccentricities which are astrophysically more probable, found that a quadrupolar template was effective in capturing a circular signal. When the next higher order post-newtonian templates are used to repeat the comparison in [51] , the matches turned out to be lower, indicating that a quasicircular template may not suffice to detect inspiral of an eccentric binary. However this was done for stellar mass black holes. What would happen in the case of massive and intermediate mass black hole binaries that are eccentric in the LIGO band? Would a numerical-relativity guided template be effective in capturing such a merger/ringdown signal resulting from an eccentric binary?

We examined this question using numerical relativity waveforms from eccentric binaries ranging from quasicircular up to high eccentricities. We found that the signal to noise among different eccentric binaries seemed to peak at $e = 0.5$, the eccentricity beyond which there seemed to be only a plunge phase. This results in being able to see an eccentric event with eccentricities in the regime $(0.4, 0.55)$ farther out than one can see a circularised binary. Then we calculated the fitting factors between the eccentric waveforms and circular templates and found that for higher masses $M > 100M_{\odot}$, the fitting factors could be as high as 0.97 for eccentricities up to 0.4, while at moderate masses of $60M_{\odot}$, the fitting factors would be > 0.95 for $e < 0.15$.

It is important to note that these eccentricities are almost the final eccentricities, at the endpoint of the evolution of the binary, and an unambiguous definition of these eccentricities in the merger regime is not available. So it would not be fair to compare these eccentricity values to those in [36] or [51] papers, as those eccentricities will circularise much faster.

Also the fitting factors they calculate are, in the parlance of [55] typical matches or best matches, instead of minimax matches which we calculate. It would be interesting to see how their numbers change when the fitting factor is changed from typical to minimax match value.

One would expect that closer one gets to the merger, the higher modes dominate and this should break the degeneracy between eccentric and non-eccentric waveforms. The higher modes become more significant as the masses increase leading to reduced fitting factors. At high masses the degeneracy is broken even with just the dominant mode alone. At low masses the higher harmonics do not carry a significant fraction of the signal-to-noise and hence, atleast heuristically we do not expect our inferences to change by much.

It is indeed somewhat surprising that a LIGO data analysis pipeline based on complete (inspiral+merger/ringdown) waveforms that are based on numerical relativity ones, would be quite effective in detection of the last few orbits of eccentric binaries. While one could argue that this can be qualitatively seen from the circularisation of the plunge and the apparent universality in the last phase of the eccentric binaries, the mass range of $20-60M_{\odot}$ still remains in need of investigation. This will lead to one more source of error in the parameter estimation and source characterisation owing to the effectualness and faithfulness of the circular templates even when matched to eccentric signals. In a certain sense LIGO will be blind, (or rather deaf) to only very high eccentricities. All moderate to low eccentricities ($e < 0.1$) for intermediate mass binaries ($60 \leq M/M_\odot \leq 300$), would be detected in the searches by quasicircular templates. The quasicircularity of the templates used in detection would cause a bias in the estimated parameters of the binary such as the mass owing to the correlation of the eccentricity with other parameters, and how this result changes with inclusion of higher harmonics will need more study. This analysis and conclusions are with non-spinning, equal mass waveforms, and the generic case spin of detection of the merger of an unequal mass binary with spin and eccentricity will attract quite some attention over the few years.

Chapter 8

Summary and Future work

...

The woods are lovely, dark and deep,

But I have promises to keep,

And miles to go before I sleep,

And miles to go before I sleep.

Robert Frost

8.1 Summary

The objective of this thesis has been to take the first steps toward using the binary black hole merger waveforms generated from numerical relativity simulations for gravitational wave observations. We investigated the accuracy requirement posed by the matched filtering detection method as well as properties of waveforms from spinning as well as eccentric binaries.

We found that while significant accuracy may be required to use the waveforms for lower mass binaries, the highest accuracies attainable are good enough to give negligible detection losses. The higher the inclination of the observer in the source frame, greater is the accuracy required because the higher modes dominate over the quadrupole mode.

We investigated the contribution of individual modes to the signal-to-noise ratio from the last orbits, merger and ringdown of a binary black coalescence. We studied two types of data, spinning binaries in circular orbits (A and B-series) and non-spinning binaries in eccentric orbits (E-series). They have equal-mass black holes with equal, initial spin magnitudes. The spins are anti-aligned with each other. In the A-series, the spins were kept parallel to the direction of the orbital angular momentum, but the magnitude of the spins varied. In the B-series, the magnitude was kept fixed to $a = 0.6$, but the initial angle the spins make with the orbital angular momentum varied. In the E-series, one measure of the initial eccentricity is varied, while the holes are initially non-spinning.

As for the case of eccentric runs from the E-series, we studied the final spin, mode content and the signal-to-noise ratio in their radiation. We found that the final state of the binary only weakly depended on the eccentricity up to significant eccentricities e 0.4. At this point the binary begins to enter a *universal* plunge before the amplitude of the gravitational radiation reaches its peak. For these eccentric binaries we found that the quadrupole mode dominated the signal-to-noise ratio, but the signal carried in higher modes did depend on the source parameters non-trivially. There was a somewhat unexpected result that for high masses, significant eccentricities in the last few orbits can be captured by a non-eccentric detection template.

8.2 Directions for future work

The promise of numerical relativity solution of the two body general relativistic problem having been fulfilled, there is a huge parameter space of initial configurations that will need to be explored in order to ensure that a possible astrophysical binary black hole merger is reliably detected. The availability of waveforms opens up a plethora of possibilities including testing general relativity in the strong field regime, a deeper understanding of the merger history of galaxies which involves formation of intermediate mass black holes, and with space based detectors even a deeper insight into the structure formation in dark matter halos and the nature of dark energy.

The work contained here dealt exclusively with initial LIGO and equal mass binaries, owing to the availability of the corresponding waveforms. The generalisation to include other noise profiles such as advanced LIGO or LISA is trivial and would not really change the qualitative conclusions. However, one important question that needs to be addressed for these cases is how effectively can the parameters of the source be characterised by using these numerical waveforms by the different detectors, and the corresponding distance reach as a function of the initial parameters.

As for the space based detectors, untangling the signals of stellar or intermediate mass binaries from the signal-dominated data stream would be another challenge, which if tackled can give lot of information on the detailed merger tree dynamics of galaxy mergers. Since the energy radiated can be maximum in certain initial configurations, such as the spins parallel to the orbital axis, such configurations may be visible further out than other configurations, introducing a bias in the detection probability for different initial configurations. A simple case for ground based detectors in the case of a generic spinning binary merger is under investigation and a factor of two increase in detection volume and hence detection rate for certain configurations is estimated. It would be interesting to develop this into a formalism for testing the so called "wet-merger" scenario that predicts that the final spins before merger would be aligned if the binary is surrounded by accreting matter, and not aligned in absence of such matter. If it is possible to distinguish the merger waveforms from these configurations one could then characterise not only the binary but also possibly their environment.

The last few cycles of merger could be a strong source for burst searches in ground based detectors and it would be interesting to see how well can one characterise the source. Whether one can distinguish a supernova burst waveform from a heavy IMBH binary merger waveform can be an interesting question for example. One could further ask on this lines how well do the burst searches characterise the merger phase and how the matched filtering performance compares to them.

Another interesting avenue is the construction of the so-called hybrid templates, which combine the post-Newtonian inspiral waveforms and the numerical merger waveforms for a search strategy. A comparison of a spin aligned waveform with the post-Newtonian counterpart could be important for extending the detection range for spinning binary black holes too.

If there are reliable astrophysical mechanisms to give significant eccentricity in the last few orbits of an IMBH binary, then this would further require extending the analysis here by inclusion of eccentric merger waveforms as templates.

One area which is as yet untouched is construction of a detection strategy for a purely numerical waveform. The template layout for post-Newtonian waveforms is possible because their dependence on all the various source parameters is known analytically. In the absence of such an analytical waveform, there have been attempts to construct phenomenological waveforms by Buonanno et al, Ajith et al etc. The question is given the numerical waveforms from a set of different initial configurations, such as some arbitrary spin orientations, arbitrary spin magnitudes and say eccentricity, it may be possible to generate some interpolating function that could give the waveform from a generic set of parameters, and such a function could then be used to set up a template grid for efficient detection.

It is an exciting time for the emerging field of gravitational wave astronomy as we work toward first direct detection of black holes, and hopefully this new window to the universe will bring with it fresh surprises, insights and challenges to keep us busy in the years to come.

References

[1] P. Ajith, S. Babak, Y. Chen, M. Hewitson, B. Krishnan, J. T. Whelan, B. Bruegmann, P. Diener, J. Gonzalez, M. Hannam, S. Husa, M. Koppitz, D. Pollney, L. Rezzolla, L. Santamaria, A. M. Sintes, U. Sperhake, and J. Thornburg. Phenomenological template family for black-hole coalescence waveforms. *arXiv.org:0704.3764*, 2007.

[2] Peter Anninos, David Hobill, Edward Seidel, Larry Smarr, and Wai-Mo Suen. The collision of two black holes. *Phys. Rev. Lett.*, 71:2851–2854, 1993.

[3] T. Apostolatos, C. Cutler, G. Sussman, and K. Thorne. Spin-induced orbital precession and its modulation of the gravitational waveforms from merging binaries, *Phys. Rev. D*, 49:6274, 1994.

[4] , F. Pretorius. Evolution of Binary Black-Hole Spacetimes. *Phys. Rev. lett.*,95:121101,2005.

[5] A. Buonanno and T. Damour. Transition from inspiral to plunge in binary black hole coalescences. Phys. Rev. D, 62:0640015,2000.

[6] M. Boyle, A. Buonanno, L. Kidder, A. H. Mroue, Y. Pan, H. P. Pfeiffer and M. A. Scheel. High-accuracy numerical simulation of black-hole binaries: Computation of the gravitational-wave energy flux and comparisons with post-Newtonian approximants, *arXiv.org:0804.4184*,

[7] P. Anninos, R. H. Price, J. Pullin, E. Seidel, W. M. Suen. Head-on collision of two black holes: Comparison of different approaches, *Phys. Rev. D* 52:4462, 1995.

[8] S. Husa, M. Hannam, J. A. Gonzalez, U. Sperhake, B.Brugmann. Reducing eccentricity in black-hole binary evolutions with initial parameters from post-Newtonian inspiral, *preprint (arXiv:0706.0904)*.

[9] C. Konigsdorffer and A. Gopakumar. Phasing of gravitational waves from inspiralling eccentric binaries at the third-and-a-half post-Newtonian order, *Phys. Rev. D* 73:124012, 2006.

[10] , B. Bruegmann, W. Tichy, N.Jansen", Numerical simulation of orbiting black holes, *Phys. Rev. lett.*,92:211101,2004.

[11] Theocharis A. Apostolatos. Search templates for gravitational waves from precessing, inspiraling binaries. *Phys. Rev. D*, 52(2):605–620, Jul 1995.

[12] P. J. Armitage and P. Natarajan. Eccentricity of Supermassive Black Hole Binaries Coalescing from Gas-rich Mergers. *Ap. J.*, 634:921–927, December 2005.

[13] Nicolas Arnaud, Matteo Barsuglia, Marie-Anne Bizouard, Violette Brisson, Fabien Cavalier, Michel Davier, Patrice Hello, Stephane Kreckelbergh, and Edward K. Porter. An elliptical tiling method to generate a 2-dimensional set of templates for gravitational wave search. *Phys. Rev. D*, 67:102003, 2003.

[14] Abhay Ashtekar and Badri Krishnan. Isolated and dynamical horizons and their applications. *Living Rev. Rel.*, 7:10, 2004.

[15] J. G. Baker, J. Centrella, D. Choi, M. Koppitz, and J. van Meter. Binary black hole merger dynamics and waveforms. *Phys. Rev. D*, 73:104002, 2006.

[16] J. G. Baker, J. Centrella, D. Choi, M. Koppitz, and J. van Meter. Gravitational wave extraction from an inspiraling configuration of merging black holes. *Phys. Rev. Lett.*, 96:111102, 2006.

[17] John G. Baker, Joan Centrella, Dae-Il Choi, Michael Koppitz, and James van Meter. Binary black hole merger dynamics and waveforms. *Phys. Rev.*, D73:104002, 2006.

[18] T. Baumgarte, P. Brady, J. Creighton, L. Lehner, F. Pretorius, and R. DeVoe. Learning about compact binary merger: the interplay between numerical relativity and gravitational-wave astronomy. *gr-qc/0612100*, 2006.

[19] E. Berti, V. Cardoso, J. A. Gonzalez, U. Sperhake, and B. Bruegmann. Multipolar analysis of spinning binaries, 2007.

[20] E. Berti, V. Cardoso, J. A. Gonzalez, U. Sperhake, M. Hannam, S. Husa, and B. Brügmann. Inspiral, merger, and ringdown of unequal mass black hole binaries: A multipolar analysis. *Phys. Rev. D*, 76(6):064034–+, September 2007.

[21] Emanuele Berti, Vitor Cardoso, and Clifford M. Will. On gravitational-wave spectroscopy of massive black holes with the space interferometer lisa. *Phys. Rev. D*, 73:064030, 2006.

[22] Emanuele Berti, Vitor Cardoso, and Clifford M. Will. On gravitational-wave spectroscopy of massive black holes with the space interferometer lisa. *Phys. Rev. D*, 73:064030, 2006.

[23] M. Campanelli, C. O. Lousto, P. Marronetti, and Y. Zlochower. Accurate evolutions of orbiting black-hole binaries without excision. 2005.

[24] J. Creighton. Search techniques for gravitational waves from black-hole ringdowns. *Phys. Rev. D*, 60:022001, 1999.

[25] C. Cutler and E. E. Flanagan. An overview of gravitational-wave sources. *Phys. Rev.*, D49:2658, 1994.

[26] Curt Cutler, Theocharis A. Apostolatos, Lars Bildsten, Lee Samuel Finn, Eanna E. Flanagan, Daniel Kennefick, Dragoljubov M. Markovic, Amos Ori, Eric Poisson, Gerald Jay Sussman, and Kip S. Thorne. The last three minutes: Issues in gravitational wave measurements of coalescing compact binaries. *Phys. Rev. Lett.*, 70:2984, 1993.

[27] Thibault Damour, Bala R. Iyer, and B. S. Sathyaprakash. Improved filters for gravitational waves from inspiralling compact binaries. *Phys. Rev. D*, 57:885, 1998.

[28] F. Echeverria. Gravitational-wave measurements of the mass and angular momentum of a black hole. *Phys. Rev. D*, 40:3194–3203, 1989.

[29] Lee Samuel Finn. Detection, measurement and gravitationfinal radiation. *Phys. Rev. D*, 46:5236, 1992.

[30] E. Flanagan and S. Hughes. Measuring gravitational waves from binary black hole coalescences: I. signal to noise for inspiral, merger, and ringdown. *Phys. Rev. D*, 57:4535–4565, 1998.

[31] E. Flanagan and S. Hughes. Measuring gravitational waves from binary black hole coalescences: II. the waves' information and its extraction, with and without templates. *Phys. Rev. D*, 57:4566–4587, 1998.

[32] J. A. Gonzalez, M. D. Hannam, U. Sperhake, B. Brugmann, and S. Husa. Supermassive recoil velocities for binary black-hole mergers with antialigned spins. *Phys. Rev. Lett.*, 98:231101, 2007.

[33] Frank Herrmann, Ian Hinder, Deirdre Shoemaker, Pablo Laguna, and Richard A. Matzner. Gravitational recoil from spinning binary black hole mergers. *Ap. J.*, 661:430–436, 2007.

[34] Frank Herrmann, Ian Hinder, Deirdre M. Shoemaker, Pablo Laguna, and Richard A. Matzner. Binary black holes: Spin dynamics and gravitational recoil. *Physical Review D (Particles, Fields, Gravitation, and Cosmology)*, 76(8):084032, 2007.

[35] R.N. Hulse and J.H. Taylor. *Astrophys. J.*, 195:L51–L53, 1975.

[36] Karl Martel and Eric Poisson. Gravitational waves from eccentric compact binaries: Reduction in signal-to-noise ratio due to nonoptimal signal processing. *Physical Review D*, 60:124008, 1999.

[37] M. Miller. Accuracy requirements for the calculation of gravitational waveforms from coalescing compact binaries in numerical relativity. *Phys. Rev. D*, 71:104016, 2005.

[38] M. C. Miller and D. P. Hamilton. Four-Body Effects in Globular Cluster Black Hole Coalescence. *Ap. J.*, 576:894–898, September 2002.

[39] Soumya D. Mohanty. Hierarchical search strategy for the detection of gravitational waves from coalescing binaries: Extension to post-newtonian wave forms. *Phys. Rev. D*, 57:630, 1998.

[40] Hiroyuki Nakano, Hirotaka Takahashi, Hideyuki Tagoshi, and Misao Sasaki. An improved search method for gravitational ringing of black holes. *Progress of Theoretical Physics*, 111:781, 2004.

[41] B. Owen. Search templates for gravitational waves from inspiraling binaries: Choice of template spacing. *Phys. Rev. D*, 53:6749–6761, 1996.

[42] Benjamin J. Owen and B. S. Sathyaprakash. Matched filtering of gravitational waves from inspiraling compact binaries: Computational cost and template placement. *Phys. Rev. D*, 60:022002, 1999.

[43] Yi Pan, Alessandra Buonanno, John G. Baker, Joan Centrella, Bernard J. Kelly, Sean T. McWilliams, Frans Pretorius, and James R. van Meter. A data-analysis driven comparison of analytic and numerical coalescing binary waveforms: nonspinning case. *arXiv:0704.1964*, 2007.

[44] A. Buonanno, T. Damour. A two body approach to general relativistic analytic two-body dynamics *Phys. Rev. D*, 59:084006, 2007.

[45] P. C. Peters. Gravitational radiation and the motion of two point masses. *Phys. Rev.*, 136:B1224–B1232, 1964.

[46] F. Pretorius. Evolution of binary black hole spacetimes. *Phys. Rev. Lett.*, 95:121101, 2005.

[47] L.F. Richardson. The approximate solution by finite differences of phys. problems involving differential equations, with an application to stresses in a masonry dam. *Phil. Trans. Roy. Soc.*, 210:307–357, 1910.

[48] B. S. Sathyaprakash. Filtering post-newtonian gravitational waves from coalescing binaries. *Phys. Rev. D*, 50:7111, 1994.

[49] B. S. Sathyaprakash and S. V. Dhurandhar. *Phys. Rev. D*, 44:3819, 1991.

[50] Jeremy D. Schnittman, Alessandra Buonanno, James R. van Meter, John G. Baker, William D. Boggs, Joan Centrella, Bernard J. Kelly, and Sean T. McWilliams. Anatomy of the binary black hole recoil: A multipolar analysis. *Physical Review D (Particles, Fields, Gravitation, and Cosmology)*, 77(4):044031, 2008.

[51] M. Tessmer and A. Gopakumar. Gravitational waves from compact binaries inspiralling along post-newtonian accurate eccentric orbits: Data analysis implications, 2007.

[52] Yoshiki Tsunesada, Nobuyuki Kanda, Hiroyuki Nakano, Daisuke Tatsumi, Masaki Ando, Misao Sasaki, Hideyuki Tagoshi, and Hirotaka Takahashi. On detection of black hole quasi-normal ringdowns: Detection efficiency and waveform parameter determination in matched filtering. *Phys. Rev. D*, 71:103005, 2005.

[53] B. Vaishnav, I. Hinder, F. Herrmann, and D. Shoemaker. Matched filtering of numerical relativity templates of spinning binary black holes. *Phys. Rev. D*, 76:084020, 2007.

[54] B. Vaishnav, D. Shoemaker, and S. Larson. The impact of finite-differencing errors on binary black hole merger templates. In *Proceeding of the 6th Annual International LISA Symposium*, 2006.

[55] Birjoo Vaishnav, Ian Hinder, Frank Herrmann, and Deirdre Shoemaker. Matched filtering of numerical relativity templates of spinning binary black holes. *Physical Review D (Particles, Fields, Gravitation, and Cosmology)*, 76(8):084020, 2007.

[56] Chris Van Den Broeck. Binary black hole detection rates in inspiral gravitational wave searches. *Class. and Quan. Grav.*, 23:L51, 2006.

[57] Chris Van Den Broeck and Anand S. Sengupta. Binary black hole spectroscopy. *Class. and Quan. Grav.*, 24:1089, 2007.

[58] Chris Van Den Broeck and Anand S. Sengupta. Phenomenology of amplitude corrected post-newtonian gravitational waveforms for compact binary inspiral. i. signal-to-noise ratios. *Class. and Quan. Grav.*, 24:155, 2007.

[59] L. Wen. On the Eccentricity Distribution of Coalescing Black Hole Binaries Driven by the Kozai Mechanism in Globular Clusters. *Ap. J.*, 598:419–430, November 2003.

[60] F.J. Zerilli. Effective potential for even-parity Regge-Wheeler gravitational perturbation equations. *Phys. Rev. Lett.*, 24:737, 1970.

Vita

Birjoo Vaishnav did his early education in Mumbai, India. After high school he won a prestigious fellowship to the Indian Institute of Technology at Kharagpur where he studied physics and specialized in quantum field theory for his final thesis. He came to Penn State to study gravity theory at the Institute of Gravitation and Cosmos, then called the Institute for Gravitational Physics and Geometry. He had a brief stint as an experimentalist designing the initial stages of a neutral atom quantum computer for a couple of years. He later switched back to theory and conducted thesis research in the emerging field of gravitational wave astronomy of merging binary black holes. While not thinking about gravitational waves he is actively involved in the campaign for a "Stress-free Violence-free Society" jointly conducted by the International Association for Human Values and the Art of Living Foundation.